J. Fluid Mech. (2001), *vol.* 433, *pp.* 209–250. Printed in the United Kingdom

On numerical stability analysis of double-diffusive convection in confined enclosures

By M. MAMOU[1], P. VASSEUR[2] AND M. HASNAOUI[3]

[1]Institute for Aerospace Research, National Research Council, Ottawa, Ontario, K1A 0R6, Canada

[2]Department of Mechanical Engineering, Ecole Polytechnique of Montreal, C.P. 6079, Succ. 'Down-Town' Montreal, Quebec, H3C 3A7, Canada

[3]Physics Department, MFE Laboratory, Faculty of Sciences Semlalia, BP 2390, Marrakesh, Morocco

(Received 7 June 1999 and in revised form 23 October 2000)

The onset of thermosolutal convection and finite-amplitude flows, due to vertical gradients of heat and solute, in a horizontal rectangular enclosure are investigated analytically and numerically. Dirichlet or Neumann boundary conditions for temperature and solute concentration are applied to the two horizontal walls of the enclosure, while the two vertical ones are assumed impermeable and insulated. The cases of stress-free and non-slip horizontal boundaries are considered. The governing equations are solved numerically using a finite element method. To study the linear stability of the quiescent state and of the fully developed flows, a reliable numerical technique is implemented on the basis of Galerkin and finite element methods. The thresholds for finite-amplitude, oscillatory and monotonic convection instabilities are determined explicitly in terms of the governing parameters. In the diffusive mode (solute is stabilizing) it is demonstrated that overstability and subcritical convection may set in at a Rayleigh number well below the threshold of monotonic instability, when the thermal to solutal diffusivity ratio is greater than unity. In an infinite layer with rigid boundaries, the wavelength at the onset of overstability was found to be a function of the governing parameters. Analytical solutions, for finite-amplitude convection, are derived on the basis of a weak nonlinear perturbation theory for general cases and on the basis of the parallel flow approximation for a shallow enclosure subject to Neumann boundary conditions. The stability of the parallel flow solution is studied and the threshold for Hopf bifurcation is determined. For a relatively large aspect ratio enclosure, the numerical solution indicates horizontally travelling waves developing near the threshold of the oscillatory convection. Multiple confined steady and unsteady states are found to coexist. Finally, note that all the numerical solutions presented in this paper were found to be stable.

1. Introduction

Thermosolutal convection has received considerable attention recently, owing to its relevance in many natural and engineering applications such as crystal growth, liquid gas storage, solar ponds and metal solidification processes (see for instance Huppert & Turner 1981 and Turner 1985). Earlier studies on double-diffusion were performed in order to explain certain geophysical phenomena. As a result, emphasis was placed

on the onset of motion in an infinite layer stratified vertically by temperature and solute concentration. A literature review demonstrates that most studies concerning thermosolutal convection are devoted to the case of an infinite horizontal layer with stress-free horizontal top and bottom boundaries. The case with rigid boundaries has received less attention since analytical solutions for this situation are considerably more difficult to obtain. However, the study of models including this last type of boundary conditions is important since they are more appropriate to many practical situations. The lack of analytical and numerical results on the stability analysis of double-diffusive convection, in confined containers with rigid boundaries, has motivated the present work. Reliable analytical and numerical techniques are introduced and some new results are presented to illustrate the effects of the non-slip boundaries and the different governing parameters on the flow behaviour.

The following literature review is focused on double-diffusive convection in horizontal fluid layers subject to vertical temperature and concentration gradients. In the early work of Stern (1960), monotonic instability for thermohaline convection in a horizontal fluid layer with stress-free boundary conditions was discussed. The possibility of oscillatory convection was reported by Lieber & Rintel (1963). Studying finite-amplitude convection, Veronis (1965) has demonstrated that subcritical instabilities may set in at a Rayleigh number smaller than that given by monotonic instability theory. Using linear stability analysis, Nield (1967) determined the thresholds for monotonic and oscillatory convection in terms of the governing parameters and for various boundary conditions. Later, Veronis (1968) and Baines & Gill (1969) used linear stability theory to investigate the case of shear-free and perfectly conducting boundaries in an infinite horizontal fluid layer. Two distinct double-diffusive convective modes were identified by these authors. The threshold for finite-amplitude convection was obtained by Veronis (1968) using a truncated representation of Fourier series.

Huppert & Moore (1976) studied the transition from oscillatory convection to finite-amplitude steady flows. For a given solutal Rayleigh number, symmetrical oscillations are observed below the threshold for monotonic instability. As the thermal Rayleigh number is increased the oscillations amplitude grows and then the flow bifurcates toward a steady convective state. Before reaching the steady state, asymmetric and aperiodic oscillations were observed. Oscillatory flows in double-diffusive convection have been considered by Da Costa, Knobloch & Weiss (1981). The threshold for finite-amplitude convection was determined and the transition between the oscillatory and steady convective modes was studied. Knobloch & Proctor (1981) investigated nonlinear convection and an analytical solution was derived in the limit where the onset of marginal overstabilities just precedes the exchange of stabilities. It was demonstrated that a subcritical steady solution branch occurs when the period of oscillations becomes infinite. Also, steady convective motion in a fluid layer with an unstable thermal and stable salinity stratification has been studied by Proctor (1981) using a perturbation analysis valid for large Lewis number. It was reported that, for any value of the solutal Rayleigh number, finite-amplitude convection can occur at values of the thermal Rayleigh number much less than that necessary for infinitesimal oscillations. An extensive review of the literature on double-diffusive convection was conducted by Huppert & Turner (1981). Travelling, standing, modulated and chaotic waves in thermosolutal convection have been demonstrated numerically by Deane, Knobloch & Toomre (1987). Transition between the oscillatory and steady convection was investigated.

Asymmetric oscillations in thermosolutal convection were observed by Moore, Weiss & Wilkins (1991) in a horizontal layer with ideal boundary conditions. For large Lewis numbers, the stability of salt fingers generated when warm salty water

lies above cool fresh water was considered by Howard & Veronis (1992). It was demonstrated that if long fingers exist, the direct instabilities are pertinent. On the other hand, if the fingers are short, the fluid traverses the finger zone before an instability could manifest itself. Experimental and numerical studies on binary fluid convection have been conducted in a thin (Hele-Shaw) isothermal rectangular cell by Predtechensky *et al.* (1994). Gel-filled membranes were used to maintain constant concentrations at the boundaries. When the lower diffusing component is stabilizing, travelling waves with high reflection coefficient at the ends of the cell appear in the system. Recently, Spina, Toomre & Knobloch (1998) obtained multiple confined states in large-aspect-ratio thermosolutal convection. Near the threshold of overstabilities, nonlinear travelling waves in the horizontal direction were observed. The travelling waves are described by a series of confined states characterized by locally enhanced heat and mass transfer.

The present paper describes a numerical and analytical investigation on the stability of double-diffusive convection in a rectangular enclosure subject to vertical gradients of heat and solute. The effects of the governing parameters and the ideal and experimental boundary conditions on the threshold of oscillatory flows and finite-amplitude convection are studied. In particular, the effects of lateral boundaries on the double-diffusive stability characteristics and finite-amplitude flow field, are investigated.

The layout of the paper is as follows. In the next section, § 2, we define the physical system and introduce the mathematical model. The numerical procedure used to solve the full governing equations is discussed in § 3. Linear and nonlinear stability analyses are carried out in § 4 to predict the critical Rayleigh numbers for the onset of subcritical, oscillatory and monotonic convection. Some results and discussion are presented in § 5. Finally, some conclusions from the present investigation are reported in § 6.

2. Mathematical model

The flow configuration under study is a two-dimensional horizontal enclosure of height H' and width W' filled with a binary fluid. The origin of the coordinate system is located at the centre of the enclosure with x' and z' being the horizontal and vertical coordinates, respectively. The two vertical boundaries of the cell are assumed rigid, impermeable and adiabatic while Dirichlet or Neumann boundary conditions are applied, for both temperature and concentration, to the horizontal walls. The binary fluid is modelled as a Newtonian Boussinesq incompressible fluid whose density, ρ, varies linearly with temperature, T', and solute concentration, S', as $\rho = \rho_0[1 - \beta_T(T' - T_0') - \beta_S(S' - S_0')]$, where ρ_0 is the density at reference temperature $T' = T_0'$ and solute concentration $S' = S_0'$, β_T and β_S being the thermal and solutal expansion coefficients, respectively, and subscript 0 denotes a reference state.

The dimensionless equations describing conservation of momentum, energy and solute are written, using the stream function formulation, as

$$\left.\begin{aligned} \frac{\partial \nabla^2\psi}{\partial t} - J(\psi, \nabla^2\psi) &= Pr\,\nabla^4\psi - Pr\left(Ra_T\frac{\partial\theta}{\partial x} + \frac{Ra_S}{Le}\frac{\partial\phi}{\partial x}\right), \\ \frac{\partial\theta}{\partial t} + \frac{\partial\psi}{\partial x} - J(\psi,\theta) &= \nabla^2\theta, \\ \frac{\partial\phi}{\partial t} + \frac{\partial\psi}{\partial x} - J(\psi,\phi) &= \frac{1}{Le}\nabla^2\phi, \end{aligned}\right\} \tag{2.1}$$

where t is the dimensionless time, ψ dimensionless stream function and θ and ϕ are respectively the temperature and concentration deviations from the rest state solution such that

$$T(t,x,z) = -z + \theta(t,x,z), \quad S(t,x,z) = -z + \phi(t,x,z); \tag{2.2}$$

here T and S are the dimensionless temperature and concentration variables. The operator J is the Jacobian defined as $J(f,g) = f_x g_z - f_z g_x$.

The dimensionless variables are obtained from $(x',z') = H'(x,z)$, $t' = tH'^2/\alpha$, $\psi' = \alpha\psi$, $S' = \Delta S^* S + S'_0$ and $T' = \Delta T^* T + T'_0$, where α is the thermal diffusivity of the binary fluid and ΔT^* and ΔS^* are the characteristic scales of temperature and concentration, respectively. The values of T'_0, S'_0, ΔT^* and ΔS^* are defined respectively by

$$\left.\begin{aligned} T'_0 &= aT'_{(0,0)} + (1-a)\frac{T'_L + T'_U}{2}, & S'_0 &= aS'_{(0,0)} + (1-a)\frac{S'_L + S'_U}{2}, \\ \Delta T^* &= a\frac{q'H'}{k} + (1-a)(T'_L - T'_U), & \Delta S^* &= a\frac{j'H'}{D} + (1-a)(S'_L - S'_U), \end{aligned}\right\} \tag{2.3}$$

where the subscript $(0,0)$ denotes the origin of the coordinate system, the subscripts L and U refer to the lower and the upper horizontal boundaries respectively, D is the mass diffusivity and k is the thermal conductivity of the fluid. The quantities q' and j' are the constant fluxes of heat and mass applied on the horizontal walls and the parameter a is set equal to zero for Dirichlet boundary conditions and to 1 for Neumann ones.

The boundary conditions on the walls are

$$\left.\begin{aligned} &\psi = \frac{\partial\psi}{\partial \boldsymbol{n}} = 0 \quad \text{on rigid boundaries,} \\ &\psi = \frac{\partial^2\psi}{\partial \boldsymbol{n}^2} = 0 \quad \text{on stress-free boundaries,} \\ &x = \pm\tfrac{1}{2}A, \quad \frac{\partial\varphi}{\partial x} = 0, \\ &z = \pm\tfrac{1}{2}, \quad a\frac{\partial\varphi}{\partial z} + (1-a)\varphi = 0, \end{aligned}\right\} \tag{2.4}$$

where φ stands for θ and ϕ and $\boldsymbol{n}$ refers to the outward boundary normal vector.

The present problem is governed by six dimensionless parameters, namely the thermal Rayleigh number, Ra_T, the solutal Rayleigh number, Ra_S, the Lewis number, Le, the aspect ratio of the enclosure, A, the Prandtl number, Pr, and the thermal and solutal boundary conditions type, a. The parameters Ra_T, Ra_S, Pr, Le and A are defined respectively as

$$Ra_T = \frac{g\beta_T \Delta T^* H'^3}{\alpha\nu}, \quad Ra_S = \frac{g\beta_S \Delta S^* H'^3}{D\nu}, \quad Pr = \frac{\nu}{\alpha}, \quad Le = \frac{\alpha}{D}, \quad A = \frac{W'}{H'}. \tag{2.5}$$

The present study will focus mainly on the case of opposing flows for which the stabilizing agent is solute ($Ra_S < 0$) and the destabilizing one is heat ($Ra_T > 0$).

The local heat and mass transfer rates expressed in terms of the Nusselt and

Sherwood numbers are given by

$$\left.\begin{aligned} Nu &= \frac{a}{T_{(x,-1/2)} - T_{(x,1/2)}} - (1-a)\frac{\partial T}{\partial z}\bigg|_{z=\pm 1/2}, \\ Sh &= \frac{a}{S_{(x,-1/2)} - S_{(x,1/2)}} - (1-a)\frac{\partial S}{\partial z}\bigg|_{z=\pm 1/2}, \end{aligned}\right\} \tag{2.6}$$

respectively.

The corresponding average values along the horizontal walls can be computed from the following integrals:

$$Nu_m = \frac{1}{A}\int_{-A/2}^{A/2} Nu\,\mathrm{d}x, \quad Sh_m = \frac{1}{A}\int_{-A/2}^{A/2} Sh\,\mathrm{d}x. \tag{2.7}$$

3. Numerical solution

In this section, the solution of the problem is obtained numerically. A finite element integration of the governing equations is considered. First a Galerkin weak formulation of the governing equations (2.1) is obtained (see Appendix A, (A 1)–(A 3)), then the calculation domain is divided into four noded rectangular elements known as the Hermite cubic elements (Reddy 1993). At each node the unknown variable (f) has four degrees of freedom: the variable itself (f), its two first derivatives (f_x and f_z) and its second cross-derivative (f_{xz}). Now using the Bubnov–Galerkin technique, the discretized governing equations are

$$\left[\frac{1}{\Delta t^0}[\boldsymbol{M}_\psi] + [\boldsymbol{C}_\psi] + Pr[\boldsymbol{K}_\psi]\right]\boldsymbol{\psi}_k^n = Pr[\boldsymbol{B}]\left(Ra_T\boldsymbol{\theta}_{k-1}^n + \frac{Ra_S}{Le}\boldsymbol{\phi}_{k-1}^n\right) + \frac{1}{\Delta t^0}[\boldsymbol{M}_\psi]\boldsymbol{\psi}^0, \tag{3.1}$$

$$\left[\frac{1}{\Delta t^0}[\boldsymbol{M}_\theta] - [\boldsymbol{C}_\theta] + [\boldsymbol{K}_\theta]\right]\boldsymbol{\theta}_k^n = \frac{1}{\Delta t^0}[\boldsymbol{M}_\theta]\boldsymbol{\theta}^0 + [\boldsymbol{L}_\theta]\boldsymbol{\psi}_{k-1}^n, \tag{3.2}$$

$$\left[\frac{1}{\Delta t^0}[\boldsymbol{M}_\phi] - [\boldsymbol{C}_\phi] + \frac{1}{Le}[\boldsymbol{K}_\phi]\right]\boldsymbol{\phi}_k^n = \frac{1}{\Delta t^0}[\boldsymbol{M}_\phi]\boldsymbol{\phi}^0 + [\boldsymbol{L}_\phi]\boldsymbol{\psi}_{k-1}^n, \tag{3.3}$$

where $[\boldsymbol{B}]$, $[\boldsymbol{C}_\psi]$, $[\boldsymbol{C}_\theta]$, $[\boldsymbol{C}_\phi]$, $[\boldsymbol{K}_\psi]$, $[\boldsymbol{K}_\theta]$, $[\boldsymbol{K}_\phi]$, $[\boldsymbol{L}_\theta]$, $[\boldsymbol{L}_\phi]$, $[\boldsymbol{M}_\psi]$, $[\boldsymbol{M}_\theta]$ and $[\boldsymbol{M}_\phi]$ are square matrices of dimension $m \times m$ ($m = 4(N_{ex}+1)(N_{ez}+1)$ is the total number of the unknown node values and N_{ex} and N_{ez} are the number of elements used in the x- and z-directions respectively). The corresponding elementary matrices are defined by (A 4). The vectors $\boldsymbol{\psi}$, $\boldsymbol{\theta}$ and $\boldsymbol{\phi}$ are unknown and are of dimension m. The parameter k refers to iteration number within each time step.

The temporal derivatives are discretized with a second backward finite difference scheme such that

$$\boldsymbol{\varphi}^0 = \tfrac{4}{3}\boldsymbol{\varphi}^{n-1} - \tfrac{1}{3}\boldsymbol{\varphi}^{n-2} \quad \text{and} \quad \Delta t^0 = \tfrac{2}{3}\Delta t, \tag{3.4}$$

where n, $n-1$ and $n-2$ correspond to times t, $t-\Delta t$ and $t-2\Delta t$ respectively, and Δt is the time step.

It is noted that, since the boundary conditions for the perturbations are homogeneous, the boundary integrals in (A 1)–(A 3), known as natural boundary conditions, vanish. In the discretized equations (3.1)–(3.3), the boundary conditions are introduced without altering the size of the matrices.

Each system of the linear equations (3.1)–(3.3) can be reduced to $[E]\boldsymbol{X} = \boldsymbol{Y}$ and

Ra_T	Pr	ψ_0	Nu_m	Sh_m
2000	1	± 4.077	1.792, 1.787^{V}	3.318, 3.307^{V}
5000	10	± 13.548	3.683, 3.681^{V}	6.493, 6.436^{V}

TABLE 1. Computed values of ψ_0, Nu_m and Sh_m for the case of an infinite horizontal layer with stress-free boundary conditions: $A = \sqrt{2}$, $Ra_S = -10^{7/2}$, $Le = 10^{1/2}$ with a grid size of $N_{ex} \times N_{ez} = 20 \times 20$. The parameter ψ_0 is the stream function value at the centre of the cell.

solved by the LU decomposition technique. To save CPU time, the Picard iterative procedure is considered. The nonlinear advective terms are treated explicitly and are included in $\boldsymbol{Y}$. At each time step, the advective terms given by the matrices $[\boldsymbol{C}_\psi]$, $[\boldsymbol{C}_\theta]$ and $[\boldsymbol{C}_\phi]$ at iteration k are evaluated using the previous results (at iteration $k-1$); likewise for the buoyancy term in (3.1) and for the linear terms associated with the matrices $[\boldsymbol{L}_\theta]$ and $[\boldsymbol{L}_\phi]$. The convergence criterion within each time step is given by

$$\frac{\sum_{i=1}^{m} (\varphi_i^k - \varphi_i^{k-1})}{\sum_{i=1}^{m} \varphi_i^k} \leqslant 10^{-8}, \tag{3.5}$$

where φ stands for ψ, θ and ϕ.

In general, depending on the governing parameter values, it was found that two to four iterations are required to satisfy the convergence criterion. A similar convergence criterion is used to obtain the steady state solution.

The grid size used in the present work was varied from 20×20 to 30×30 and the time step, Δt, from 10^{-5} to 10^{-3} depending on the values of the governing parameters. To validate our numerical code, the case of a rectangular enclosure with stress-free boundaries and Dirichlet boundary conditions for temperature and concentration ($a = 0$) is considered. An aspect ratio of $A = \sqrt{2}$ is chosen to simulate the infinite horizontal layer (see Veronis 1968). Using a grid size of 20×20 the values of the average Nusselt and Sherwood numbers are observed to agree well with the results of Veronis (1968), denoted by the superscript V in table 1, with a maximum deviation of less than 1%. These results were also reproduced by using periodic boundary conditions in the horizontal direction using an aspect ratio of $A = 2^{3/2}$.

In the present paper, all the fully developed numerical solutions (steady and oscillatory states) obtained from the full transient governing equations are found to be stable and sustainable. The stability of these solutions was demonstrated by adding infinitesimal perturbations to the converged solutions and observing how these perturbations evolve in time. For-steady state convection, it was found that, after a while, the convective flow returns to its initial converged state (the results are not presented here). Also, using a standard linear stability analysis of the steady-state solutions, it was found that the real part of the growth rate parameter is negative and the imaginary part is positive which indicates a decaying oscillatory perturbation. The stability of the oscillatory flows was also demonstrated by imposing small perturbations on the fully developed periodic solutions. In all cases, the perturbations were found to decay and the initial oscillatory periodic flow was recovered. Obviously, in regions where multiple solutions coexist, a strong perturbation (with finite-amplitude) could cause one solution to bifurcate towards the other.

4. Stability analysis

In this section, the stability analysis of three different situations is considered. The first and the second ones concern the linear stability analysis of the basic rest state solution and of the fully developed flows. The thresholds for stationary convection and oscillatory flows are determined as functions of the governing parameters. In the third situation, a weak nonlinear stability analysis is considered and the threshold for subcritical convection is obtained. The linear stability analysis of the pure diffusive state will be considered first.

4.1. *Onset of convection: linear theory*

In this section, the physical situation described by (2.1) and (2.4) is examined, now from the standpoint of stability to small perturbations from the quiescent state. At the very beginning of convection the stream function, ψ, temperature, θ, and concentration, ϕ, fields can be expressed in the usual manner as

$$\psi(t,x,z) = \psi_0\, \mathrm{e}^{pt} F(x,z), \quad \theta(t,x,z) = \theta_0\, \mathrm{e}^{pt} G(x,z), \quad \phi(t,x,z) = \phi_0\, \mathrm{e}^{pt} H(x,z), \tag{4.1}$$

where $F(x,z)$, $G(x,z)$ and $H(x,z)$ are unknown space functions describing the fields of ψ, θ and ϕ at the onset of convection, ψ_0, θ_0 and ϕ_0 are small unknown amplitudes and p is a complex number expressing the growth rate of the perturbation.

Substituting (4.1) into (2.1) and after neglecting the second-order terms (the amplitudes ψ_0, θ_0 and ϕ_0 being close to zero) it is found that

$$\left.\begin{aligned} p\,\psi_0 \nabla^2 F &= \psi_0 Pr \nabla^4 F - Pr\left(Ra_T \theta_0 \frac{\partial G}{\partial x} + \frac{Ra_S}{Le}\phi_0 \frac{\partial H}{\partial x}\right), \\ p\,\theta_0 G + \psi_0 \frac{\partial F}{\partial x} &= \theta_0 \nabla^2 G, \\ p\,\phi_0 H + \psi_0 \frac{\partial F}{\partial x} &= \frac{\phi_0}{Le}\nabla^2 H. \end{aligned}\right\} \tag{4.2}$$

The above linear perturbation equations are solved numerically using the finite element method described in the previous section. The neutral stability analysis will be considered first.

4.1.1. *Threshold of stationary convection* ($p = 0$)*: accurate approach*

In this part, a finite element technique is used to solve the linear equations, for the case of marginal stability, to determine the perturbation profiles $F(x,z)$, $G(x,z)$ and $H(x,z)$ and the threshold for the onset of monotonic convection ($p = 0$).

Following the Bubnov-Galerkin procedure, the finite element discretization of the linear equations (4.2) yields

$$\psi_0[\boldsymbol{K}_\psi]\boldsymbol{F} = [\boldsymbol{B}]\left(Ra_T \theta_0 \boldsymbol{G} + \frac{Ra_S}{Le}\phi_0 \boldsymbol{H}\right), \tag{4.3}$$

$$\psi_0[\boldsymbol{L}_\theta]\boldsymbol{F} = \theta_0[\boldsymbol{K}_\theta]\boldsymbol{G}, \tag{4.4}$$

$$\psi_0[\boldsymbol{L}_\phi]\boldsymbol{F} = \frac{\phi_0}{Le}[\boldsymbol{K}_\phi]\boldsymbol{H}, \tag{4.5}$$

where $[\boldsymbol{B}]$, $[\boldsymbol{K}_\psi]$, $[\boldsymbol{K}_\theta]$, $[\boldsymbol{K}_\phi]$, $[\boldsymbol{L}_\theta]$ and $[\boldsymbol{L}_\phi]$ are square matrices defined in (A 4) and $\boldsymbol{F}$, $\boldsymbol{G}$ and $\boldsymbol{H}$ are unknown vectors of dimension m.

Since the thermal and solutal boundary conditions are of the same type, it follows that $[\boldsymbol{K}_\theta] = [\boldsymbol{K}_\phi] = [\boldsymbol{K}]$ and $[\boldsymbol{L}_\theta] = [\boldsymbol{L}_\phi] = [\boldsymbol{L}]$. Thus, it can be observed from (4.4)

i	$a=0$	$a=1$
1	2585.0439	1684.4900
2	6742.5467	6217.4937
3	19 636.3992	16 030.9104
4	23 321.3792	18 911.2115
5	25 704.3757	19 399.4296

TABLE 2. Computed critical parameter $Ra_i^{sup} = 1/\lambda_i$ for $a = 0$ and 1 obtained for a square enclosure with rigid boundaries and $N_{ex} \times N_{ez} = 20 \times 20$. The imaginary parts of λ_i are null and the corresponding eigenfunctions are real.

and (4.5) that $\boldsymbol{H} = \boldsymbol{G}$ and $\phi_0 = Le\,\theta_0$. Upon using these relations, (4.3)–(4.5) can be combined to yield

$$\psi_0[\boldsymbol{E} - \lambda \boldsymbol{I}]\boldsymbol{F} = 0, \tag{4.6}$$

where $[\boldsymbol{I}]$ is the identity matrix, $[\boldsymbol{E}]$ is a matrix defined as $[\boldsymbol{E}] = [\boldsymbol{K}_\psi]^{-1}[\boldsymbol{B}][\boldsymbol{K}]^{-1}[\boldsymbol{L}]$ and the parameter $\lambda = 1/(Ra_T + Ra_S)$. The superscript -1 denotes the inverse of a matrix.

From a mathematical point of view, (4.6) represents an eigenvalue problem for which a non-trivial solution exists if and only if the determinant of $[\boldsymbol{E} - \lambda \boldsymbol{I}]$ is equal to zero. This leads to the computation of all the eigenvalues λ_i and the corresponding eigenvectors $\boldsymbol{F}_i$ satisfying (4.6). The computations are performed by using the subroutine DE2CRG of the IMSL library.

The eigenfunction $G(x, z)$ can be then deduced from

$$G_i = [\boldsymbol{K}]^{-1}[\boldsymbol{L}]\boldsymbol{F}_i. \tag{4.7}$$

If the eigenvalues λ_i can be rearranged in the following manner $\lambda_1 \geqslant \lambda_2 \geqslant \ldots \geqslant \lambda_{m-1} \geqslant \lambda_m$, the supercritical thermal Rayleigh number, Ra_{TC}^{sup}, for the onset of supercritical convection is then given by

$$Ra_{TC}^{sup} = -Ra_S + Ra^{sup}, \tag{4.8}$$

where the critical parameter Ra^{sup} is defined as

$$Ra^{sup} = \frac{1}{\lambda_1}. \tag{4.9}$$

Note that the other critical values, $Ra_i^{sup} = 1/\lambda_i$ with $i = 2, \ldots, m$, correspond to the onset of the higher supercritical modes. In table 2, the first five eigenvalues are given for the case of a rigid square enclosure with either Dirichlet ($a = 0$) or Neumann ($a = 1$) boundary conditions. The corresponding eigenfunctions are plotted in figure 1. It is observed that the first mode consists of one single cell. For the other modes, the incipient flows structures exhibit multicellular configurations.

The effect of the grid size on the computed value Ra^{sup} is depicted in table 3 for the case of a square enclosure with rigid boundaries and Dirichlet boundary conditions. As the grid size is reduced, the critical parameter value is seen to converge towards the one already predicted by Platten & Legros (1984). Also it is noted that the convergence rate was found to be $O(d^4)$, where d is the mesh size based on the diagonal length of an element, i.e. $d = (\Delta x_e^2 + \Delta z_e^2)^{1/2}$ and Δx_e and Δz_e are the horizontal and vertical dimensions of an element.

The case of an infinite horizontal layer will be now discussed. For this situation,

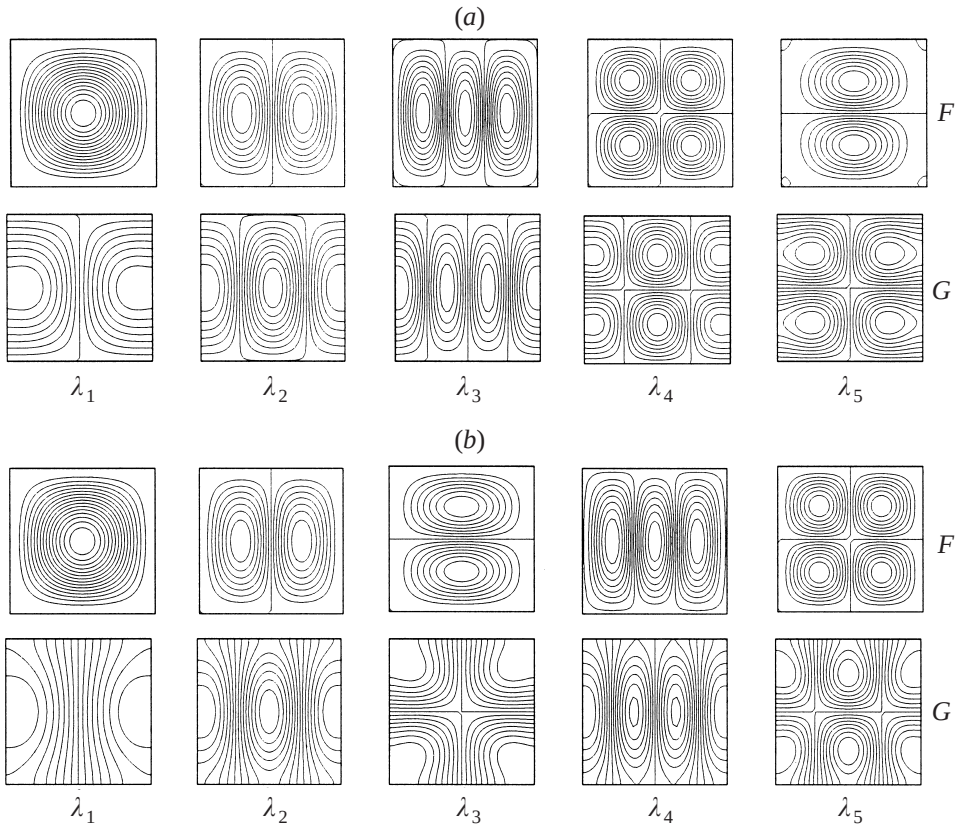

FIGURE 1. Incipient flows structures, F, temperature and concentration perturbation profiles, G, for the first five eigenvalues λ_i, obtained for a square enclosure having rigid boundaries with: (*a*) Dirichlet boundary conditions ($a = 0$), and (*b*) Neumann boundary conditions ($a = 1$).

$N_{ex} \times N_{ey}$	4×4	8×8	16×16	20×20	Platten & Legros (1984)
Ra^{sup}	2596.6699	2585.8739	2585.0790	2585.0439	2585.03

TABLE 3. Effect of the grid size on the computed value of $Ra^{sup} = 1/\lambda_1$ for $A = 1$ and $a = 0$.

periodic boundary conditions in the horizontal direction have to be considered. The perturbation solution can then be developed as

$$\psi(t, x, z) = \psi_0 \, \mathrm{e}^{pt + \mathrm{i}\omega x} F(z), \quad \theta(t, x, z) = \theta_0 \, \mathrm{e}^{pt + \mathrm{i}\omega x} G(z), \quad \phi(t, x, z) = \phi_0 \, \mathrm{e}^{pt + \mathrm{i}\omega x} H(z), \tag{4.10}$$

where ω is an unknown wavenumber defined as $\omega = 2\pi/A_C$ and A_C is the critical wavelength. Now F, G and H are functions of z only.

Upon substituting the perturbation, (4.10), into the governing equations and following the numerical technique described in § 4.1.1, one obtains linear matrix systems similar to those depicted in (4.3)–(4.5) in which the elementary matrices are given in Appendix B.

For the present situation, the critical Rayleigh number and the eigenfunctions are

computed for a given aspect ratio, A, of the enclosure as described in § 4.1.1. Varying step by step the aspect ratio of the enclosure the corresponding critical values of Ra^{sup} are computed. The minimum one then gives the critical value for the onset of stationary convection and the corresponding aspect ratio, A_C, then represents the critical wavelength of the convective rolls. An efficient automatic numerical procedure is used to search for the minimum value of Ra^{sup}. Using 40 elements in the z-direction, the computed values of Ra^{sup} and A_C for the case of a horizontal layer with rigid boundaries and $a = 0$ are 1707.7625 and 2.0160 respectively, which are in good agreement with the classical results obtained by Ried & Harris (1958).

4.1.2. *Threshold of oscillatory convection* ($p \neq 0$)*: approximate approach*

In the above section, we have demonstrated how to obtain the critical parameters for the onset of motion and the corresponding eigenfunctions $F(x, z)$ and $G(x, z)$. Since the trial functions $w(x, z)$ and $\vartheta(x, z)$ can be chosen arbitrarily in the weak Galerkin formulation, (A 1)–(A 3), they can be substituted by the functions $F(x, z)$ and $G(x, z)$, respectively, since they satisfy the boundary conditions of the problem. In this first approach, real eigenfunctions are used to determine the threshold for the overstable regime (i.e. the eigenfunctions are independent of the growth rate parameter p and they are calculated at the onset of stationary convection). Recall that, for the case of non-slip boundary conditions, the eigenfunction are complex (see, for instance, Knobloch & Moore 1988).

Performing the weighted residual technique yields the following linear equations:

$$p\mathscr{M}_\psi \psi_0 + \mathscr{K}_\psi \psi_0 = \mathscr{B}\left(Ra_T \theta_0 + \frac{Ra_S}{Le}\phi_0\right), \tag{4.11}$$

$$p\mathscr{M}\theta_0 - \mathscr{L}\psi_0 = -\mathscr{K}\theta_0, \tag{4.12}$$

$$p\mathscr{M}\phi_0 - \mathscr{L}\psi_0 = -\frac{\mathscr{K}}{Le}\phi_0, \tag{4.13}$$

where the constants $\mathscr{B}$, $\mathscr{K}_\psi$, $\mathscr{K}$, $\mathscr{L}$, $\mathscr{M}_\psi$ and $\mathscr{M}$ can be computed from Appendix C.

Solving (4.12) and (4.13) for θ_0 and ϕ_0 and substituting the resulting expressions into (4.11) yields, after some algebra, the dispersion relationship

$$Le\left(\frac{p}{\gamma}\right)^3 + p_2\left(\frac{p}{\gamma}\right)^2 - p_1\left(\frac{p}{\gamma}\right) - \sigma Pr\, p_0 = 0, \tag{4.14}$$

where

$$\begin{aligned} &p_0 = Ra_T^0 + Ra_S^0 - 1, \quad p_1 = \sigma Pr[Le(Ra_T^0 - 1) + Ra_S^0 - 1] - 1, \\ &p_2 = Le(\sigma Pr + 1) + 1, \end{aligned} \tag{4.15}$$

and

$$\left.\begin{aligned} &Ra_T^0 = \frac{Ra_T}{Ra^{sup}}, \quad Ra_S^0 = \frac{Ra_S}{Ra^{sup}}, \quad Ra^{sup} = \frac{\mathscr{K}_\psi \mathscr{K}}{\mathscr{B}\mathscr{L}}, \\ &\gamma_\psi = \frac{\mathscr{K}_\psi}{\mathscr{M}_\psi}, \qquad \gamma = \frac{\mathscr{K}}{\mathscr{M}}, \qquad \sigma = \frac{\gamma_\psi}{\gamma}. \end{aligned}\right\} \tag{4.16}$$

Here the parameters γ and σ are positive and functions of the aspect ratio of the enclosure and the boundary conditions applied to the system. From a physical point of view the parameter γ can be considered as the amplification coefficient of the amplitude growth rate p. On the other hand, the parameter σ expresses the strength

	a	γ_ψ	γ	$\sigma = \gamma_\psi/\gamma$	Ra^{sup}
RR	0	53.961	20.567	2.624	2585.079
RF	0	43.889	20.614	2.129	2023.634
FF	0	38.077	20.480	1.859	1643.830
RR	1	55.149	10.759	5.126	1684.525
RF	1	44.169	10.624	4.158	1246.518
FF	1	38.353	10.439	3.674	981.853

TABLE 4. Computed values of γ, γ_ψ, σ and Ra^{sup} for a square enclosure subject to different boundary conditions with $N_{ex} \times N_{ez} = 16 \times 16$. For this situation, the vertical boundaries are rigid.

	a	A_C	$\omega = 2\pi/A_C$	γ_ψ	γ	$\sigma = \gamma_\psi/\gamma$	Ra^{sup}
RR	0	2.0160	3.1167 (3.12)^{RH}	38.4022	19.6435	1.955	1707.7625 (1707.765)^{RH}
RF	0	2.3422	2.6826 (2.68)^{RH}	24.7451	17.1873	1.440	1100.6498 (1100.657)^{RH}
FF	0	2.8281	2.2217 (2.22)^{R}	14.8027	14.8027	1.000	657.5114 (657.511)^{R}
RR	1	∞	0.0000 (0)^{SGJ}	42.0000	0.0000	∞	720.0000 (720)^{SGJ}
RF	1	∞	0.0000 (0)^{SGJ}	21.0000	0.0000	∞	320.0000 (320)^{SGJ}
FF	1	∞	0.0000 (0)^{N}	9.8824	0.0000	∞	120.0000 (120)^{N}

TABLE 5. Computed values of A_C, γ, γ_ψ, σ and Ra^{sup} for an infinite layer subject to different boundary conditions with $N_{ez} = 40$.

of the inertial force effects on the growth rate parameter. When σ is very large the inertial effects are weak enough to be neglected.

The dispersion equation (4.14) could be solved explicitly for the growth parameter p. Depending on the governing parameters values the zeros of (4.14) can be either three real roots or one real root and two complex-conjugate roots.

At this point, in order to validate the present numerical procedure, it is worth giving some typical results for various hydrodynamic, thermal and solutal boundary conditions. The case of a square enclosure with rigid vertical boundaries and an infinite horizontal layer is considered. The lower and the upper boundaries can be either rigid–rigid (RR), rigid–free (RF) or free–free (FF). Dirichlet ($a = 0$) and Neumann ($a = 1$) boundary conditions for temperature and concentration are also considered. The values of the parameters Ra^{sup}, γ, γ_ψ and σ are reported in tables 4 and 5 for square and infinite enclosures, respectively. The critical wavelength, A_C, is also given in table 5. Table 5 shows a good agreement between the present results and those available in the literature (Rayleigh 1916 (R); Sparrow, Goldstein & Jonsson 1964 (SGJ); Reid & Harris 1958 (RH) and Nield 1967 (N).

To our knowledge, the parameters γ, γ_ψ and σ are obtained for the first time if we exclude the case of an infinite horizontal layer with stress-free and Dirichlet boundary conditions. For this situation, we can deduce from the results of Nield (1967) that $\gamma = \gamma_\psi = 3\pi^2/2$ and $\sigma = 1$ for $A = \sqrt{2}$ which agree well with the present results (see table 5).

Figure 2 illustrates the effects of the aspect ratio, A, and the boundary conditions on the parameters Ra^{sup}, γ and σ for the case of a confined enclosure with rigid vertical boundaries. The results presented in figure 2 correspond only to the first eigenvalue, λ_i. The case with Dirichlet boundary conditions ($a = 0$), is depicted in figure 2(*a–c*). For a square enclosure ($A = 1$) with rigid boundaries (RR), figure 2(*a*), the numerical results indicate that the incipient flow exhibits one convective cell and

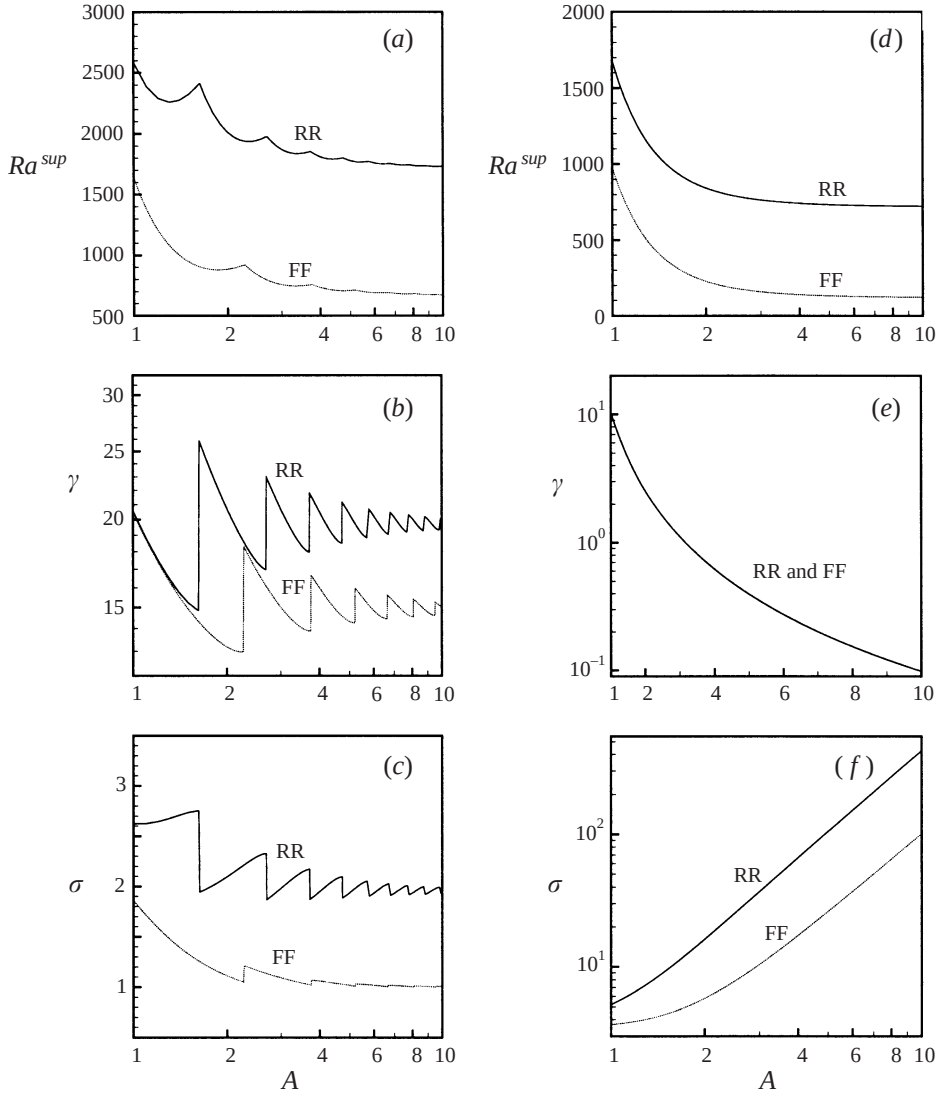

FIGURE 2. Parameters Ra^{sup}, γ and σ as functions of the aspect ratio, A, of the enclosure with rigid (RR) and free (FF) boundaries: (a–c) $a = 0$; (b–f) $a = 1$.

$Ra^{sup} = 2585.04$. As the aspect ratio is increased, Ra^{sup} is seen to decrease, passing through a minimum and then increases until $A \simeq 1.625$. As the value of A is increased above 1.625, an abrupt decrease in Ra^{sup} is observed. This is due to the fact that the flow structure changes to a two-cellular mode. On the other hand, the parameters γ and σ, in figures 2(b) and 2(c), undergo a decrease and an increase, respectively, when A rises from 1 to 1.625. At the transition point, the values of γ and σ are seen to jump up and down, respectively, as the flow structure passes from the one- to two-cell mode. At the peak ($A \simeq 1.625$), $Ra^{sup} \simeq 2414$ and the numerical results demonstrate that two solutions, with a different flow structure, are possible. Since the value of the parameter γ for the two-cell flow solution is greater than that of the one-cell flow solution, it is clear that the growth rate of the former is greater than that of the latter according to (4.14). In this situation, the threshold for the onset of the

oscillatory convection for the two-cell mode could be lower than that corresponding to the one-cell mode. As the aspect ratio is increased, the amplitudes of the peaks (figure 2*a*) and the jumps (figure 2*b*, *c*) are seen to dwindle. The asymptotic trends, observed when A is made larger, correspond to an infinite horizontal layer. For the case with free boundaries (FF), similar results are depicted in the same graphs. For Neumann boundary conditions ($a = 1$), figure 2*d–f*, the parameters Ra^{sup}, γ and σ are seen to vary monotonically with the aspect ratio A, in contrast with the previous case. This is due to the fact that, at the onset of stationary convection, the flow structure remains unicellular for any aspect ratio, such that a zero wavenumber is obtained for a horizontal infinite layer. As discussed later, the flow structure could be multicellular near the threshold of overstabilities. In addition, the parameter γ in figure 2(*e*) is seen to decrease towards zero as A is made very large. For this situation, the growth rate parameter p becomes smaller and it takes a long time for a perturbation to initiate a convective flow. On the other hand, σ is seen to increase towards infinity.

The onset of monotonic and oscillatory instabilities will be now discussed. From a mathematical point of view, according to (4.14) and (4.15) the threshold of monotonic instability is obtained when $p = 0$ (i.e. $p_0 = 0$). Thus we have

$$Ra_{TC}^{sup} = (1 - Ra_S^0)Ra^{sup}; \tag{4.17}$$

Ra_{TC}^{sup} will be referred hereafter as the supercritical Rayleigh number.

The growth rate parameter, p, is a complex number which can be decomposed as $p = p_r + \mathrm{i}p_i$, where p_r and p_i are the real and the imaginary parts, respectively. Overstability, which arises when $p_r = 0$ and $p_i \neq 0$, yields

$$p_i^2 = -\gamma^2 \frac{p_1}{Le} \quad \text{and} \quad p_i^2 = -\gamma^2 \sigma Pr \frac{p_0}{p_2}. \tag{4.18}$$

From the above expression, it is clear that the conditions $p_0 < 0$ and $p_1 < 0$ should be satisfied for the existence of the overstable regime.

Equating these two expressions for p_i and making use of (4.15), the threshold of oscillatory convection is obtained as

$$Ra_{TC}^{over} = \min\left\{\left(-\frac{1+\sigma_i PrLe}{Le^2(1+\sigma_i Pr)}Ra_S^0 + \frac{(Le+1)(1+\sigma_i PrLe)}{\sigma_i PrLe^2}\right)Ra_i^{sup}\right\}. \tag{4.19}$$

This expression is valid for any boundary conditions considered in the present work. The subscript i refers to the eigenvalues λ_i with $i = 1, \ldots, m$.

For an infinite layer, the threshold for oscillatory flow is given by $\min\{Ra_{TC}^{over}(\sigma_1, Ra_1^{sup}, A)\}$. This is obtained by varying the wavelength A until the minimum value of Ra_{TC}^{over} is obtained. The corresponding aspect ratio is then the critical wavelength.

The transition from the oscillatory to monotonically augmented convection regime is marked by the critical Rayleigh number, Ra_{TC}^{osc}, which can be obtained by setting $p_i = 0$ (i.e. $p = p_r > 0$) in (4.14). One can obtain implicitly the value of Ra_{TC}^{osc} from

$$\left.\begin{aligned} Le\left(\frac{p_r}{\gamma}\right)^3 + p_2\left(\frac{p_r}{\gamma}\right)^2 - p_1\left(\frac{p_r}{\gamma}\right) - \sigma Pr\, p_0 = 0, \\ p_r = \frac{\gamma}{3Le}\left(-p_2 + \sqrt{p_2^2 + 3Le\, p_1}\right). \end{aligned}\right\} \tag{4.20}$$

For given Ra_S, Le, Pr and A, the value of Ra_{TC}^{osc} can be computed numerically from (4.20) using, for example, the Newton-Raphson method.

The three critical Rayleigh numbers given by (4.17), (4.19) and (4.20) intersect at a point having the following coordinates:

$$\overline{Ra}_T = \frac{\sigma PrLe + 1}{\sigma Pr(Le-1)} Ra^{sup}, \quad \overline{Ra}_S = -\frac{\sigma Pr + 1}{\sigma Pr(Le-1)} Ra^{sup}. \tag{4.21}$$

This intersection point gives the limit beyond which the overstable regime can exist ($Ra_T > \overline{Ra}_T$ and $Ra_S < \overline{Ra}_S$). From the above results, it is clear that overstabilities may arise only when $Ra_S < 0$ and $Le > 1$ or when $Ra_T < 0$ and $Le < 1$.

4.1.3. *Limiting cases: $Pr \gg 1$ and $Le \gg 1$*

For large values of Pr, the critical Rayleigh numbers, given by (4.19) and (4.20), reduce to

$$\left.\begin{aligned} Ra_{TC}^{over} &= \frac{Le + 1 - Ra_S^0}{Le} Ra^{sup}, \\ Ra_{TC}^{osc} &= \frac{Le - 1 - Ra_S^0 + 2\sqrt{(1-Le)Ra_S^0}}{Le} Ra^{sup}. \end{aligned}\right\} \tag{4.22}$$

and they become independent of Pr.

For large Lewis number ($Le \to \infty$), it can be demonstrated that the threshold for the onset of overstability $Ra_{TC}^{over} \to Ra^{sup}$ as $Le \to \infty$ and the domain delineating the overstable regime becomes narrower.

4.1.4. *Threshold of oscillatory convection ($p_r = 0$ and $p_i \neq 0$): accurate approach*

For this situation, the eigenfunctions could be complex and they are functions of the growth rate parameter, p. The perturbation profiles remain the same as depicted in (4.1) for confined enclosure and in (4.10) for an infinite layer.

Using the finite element method, the discretization of the linear perturbation equations leads to the following linear system of equations:

$$\begin{bmatrix} [\mathbb{K}_\psi] & [\mathbb{B}_{\psi\theta}] & [\mathbb{B}_{\psi\phi}] \\ [\mathbb{B}_\theta] & [\mathbb{K}_\theta] & 0 \\ [\mathbb{B}_\phi] & 0 & [\mathbb{K}_\phi] \end{bmatrix} \begin{Bmatrix} \boldsymbol{F} \\ \boldsymbol{G} \\ \boldsymbol{H} \end{Bmatrix} = p \begin{bmatrix} [\mathbb{M}_\psi] & 0 & 0 \\ 0 & [\mathbb{M}_\theta] & 0 \\ 0 & 0 & [\mathbb{M}_\phi] \end{bmatrix} \begin{Bmatrix} \boldsymbol{F} \\ \boldsymbol{G} \\ \boldsymbol{H} \end{Bmatrix}. \tag{4.23}$$

The corresponding elementary matrices are defined by $[\mathbb{B}_{\psi\theta}]^e = -PrRa_T[\boldsymbol{B}]^e$, $[\mathbb{B}_{\psi\phi}]^e = -(PrRa_S/Le)[\boldsymbol{B}]^e$, $[\mathbb{M}_\psi]^e = -[\boldsymbol{M}_\psi]^e$, $[\mathbb{M}_\theta]^e = -[\boldsymbol{M}_\theta]^e$, $[\mathbb{M}_\phi]^e = -[\boldsymbol{M}_\phi]^e$, $[\mathbb{K}_\phi]^e = (1/Le)[\boldsymbol{K}]^e$ and $[\mathbb{K}_\psi] = Pr[\boldsymbol{K}_\psi]^e$, where $[\boldsymbol{B}]^e$, $[\boldsymbol{M}_\psi]^e$, $[\boldsymbol{M}_\theta]^e$, $[\boldsymbol{M}_\phi]^e$, $[\boldsymbol{K}_\psi]^e$, $[\boldsymbol{K}_\theta]^e$ and $[\boldsymbol{K}_\phi]^e$ are defined by (A 4) for confined enclosure and by (B 1) for an infinite layer.

For a given set of the governing parameters, Ra_S, Pr, Le, A and a, the eigenvalues, p, and eigenfunctions $\boldsymbol{F}$, $\boldsymbol{G}$ and $\boldsymbol{H}$ of the above system are computed using the subroutines *DGVCRG* and *DGVCCG* of the IMSL library for general real and complex matrices, respectively. The onset of oscillatory convection is obtained by only one eigenvalue when its real part changes from negative to positive values. This is obtained by varying the thermal Rayleigh number (and the wavelength for the infinite layer). The lowest Rayleigh number for any value of the wavelength then corresponds to the critical Rayleigh number. If the imaginary part of the eigenvalue is different from zero the instability is then oscillatory. It is found that, at the onset of overstability, there are two eigenvalues having zero real parts and the same imaginary parts with negative and positive values. To validate the two present approaches, the work of Spina *et al.* (1998) is considered. The values of the governing parameters are

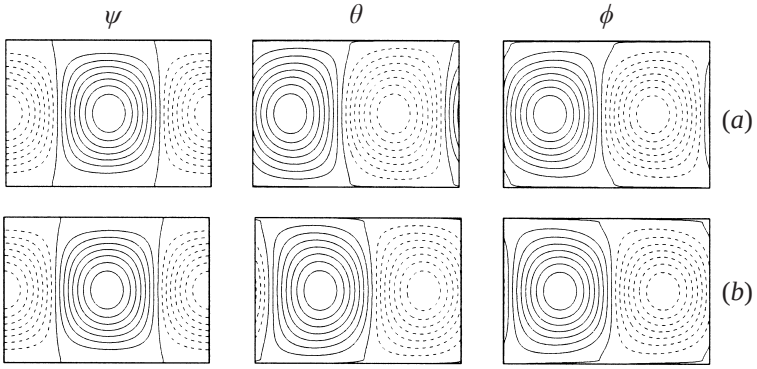

FIGURE 3. Perturbation profile at the onset of oscillatory convection in an infinite horizontal layer with non-slip boundaries for $Ra_S = -3 \times 10^{9/2}$, $Pr = 1$, $Le = 10^{1/2}$ and $a = 0$; $Ra_{TC}^{over} = 25251.75$, $A_C = 1.4369$: (*a*) $p_i = 70.656$ and (*b*) $p_i = -70.65$.

	Approximate approach	Accurate approach	Spina *et al.* (1998)
Ra_{TC}^{over}	24 987.05	25 251.75	25 251.76
A_C	1.460	1.4369	1.4378
p_i	± 69.92	± 70.656	70.66

TABLE 6. Critical Rayleigh number, Ra_{TC}^{over}, critical wavelength, A_C, and oscillation frequency, p_i, at the onset of the overstable regime for $Ra_S = -3 \times 10^{9/2}$, $Pr = 1$, $Le = 10^{1/2}$ and $a = 0$ in an infinite horizontal layer with rigid boundaries ($N_{ey} = 20$).

$Ra_S = -3 \times 10^{9/2}$, $Pr = 1$, $Le = 10^{1/2}$ and $a = 0$ with rigid boundaries. For an infinite horizontal layer, the critical Rayleigh number, Ra_{TC}^{over}, the critical wavelength, A_C, and the oscillation frequency, p_i, are depicted in table 6. The agreement between the present results with those of Spina *et al.* (1998) is excellent. However the approximate approach is seen to underestimate the accurate results within 1.5%. The difference between the two present approaches is that the approximate one assumes a vertical boundary of the cell (since the eigenfunctions are obtained at the onset of stationary convection) and the accurate one allows the vertical boundary to be bowed to the left or to the right in the horizontal direction. Also, it can be observed that the temperature and concentration are out of spatial phase, as shown in figure 3, and left ($p_i > 0$) or right ($p_i < 0$) travelling waves could develop near the threshold of oscillatory convection. The computation for the first approach, however, is much faster than the second one (i.e. the matrix dimensions of the former are 3×3 less than those of the latter).

The effect of the governing parameters Pr and Le on the threshold of oscillatory convection is examined for an infinite horizontal layer. The results are depicted in figure 4 in terms of the critical Rayleigh number, Ra_{TC}^{over}, the critical wavelength, A_C, and the oscillation frequency, p_i, for $Ra_S = -10^5$. Recall that in an infinite horizontal layer with stress-free boundaries, the critical wavelength ($A_C = 2\sqrt{2}$) is independent of the governing parameters (Veronis 1968). However, for non-slip boundaries, the critical wavelength, as shown in figure 4, is found to be a function of the governing parameters. The parameters Ra_{TC}^{over}, A_C and p_i are plotted, in figure 4, as functions of Pr for different values of Le. For Dirichlet boundary condition (figure 4*a*) when the Prandtl number is increased from 0.001 to 1000, Ra_{TC}^{over} and A_C are seen to

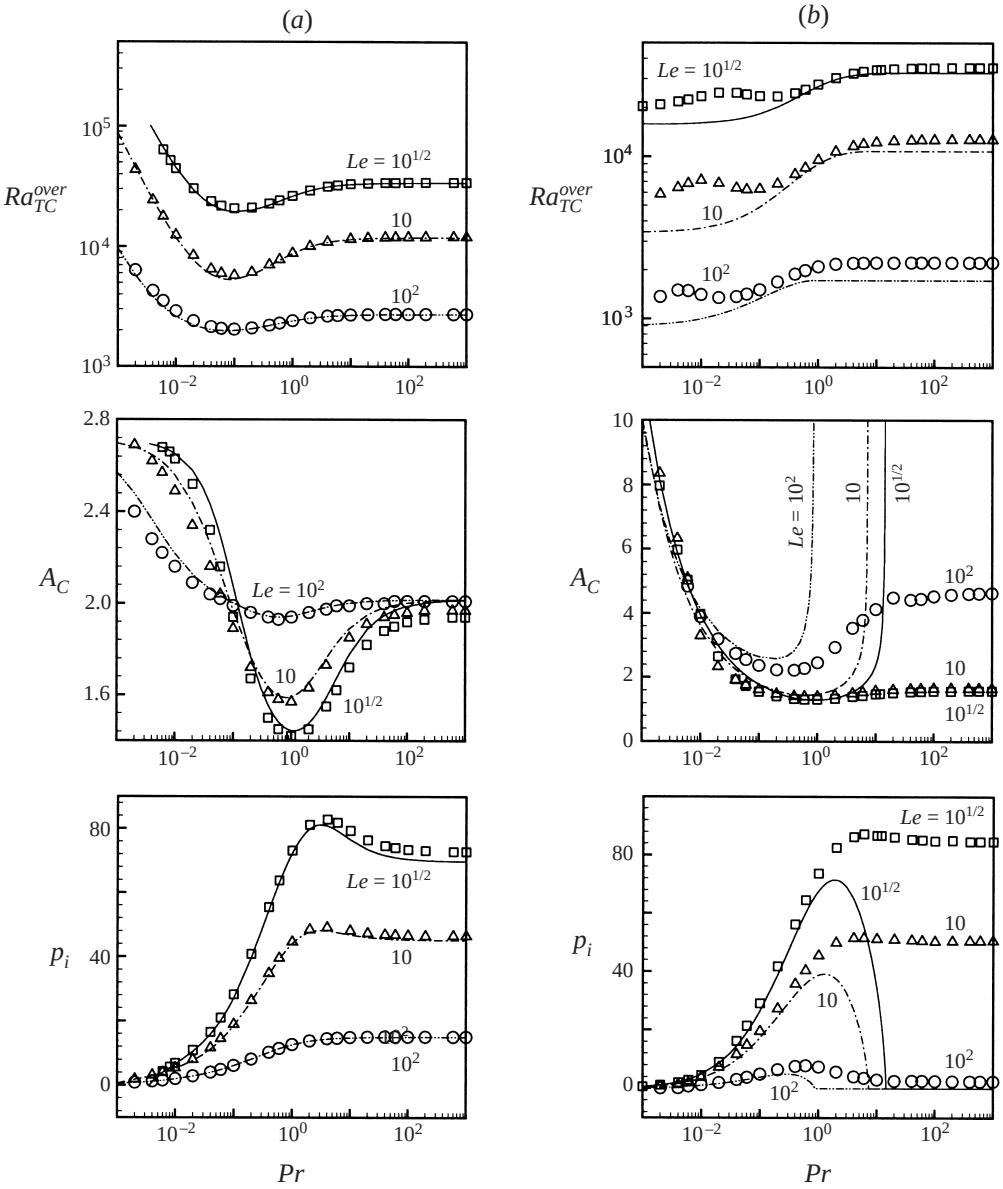

FIGURE 4. Onset of oscillatory convection: critical Rayleigh number, Ra_{TC}^{over}, critical wavelength, A_C, and oscillation frequency, p_i, as functions of Pr and Le for $Ra_S = -10^5$ in an infinite layer with non-slip boundaries; (*a*) $a = 0$ and (*b*) $a = 1$. The approximate approach is represented by lines and the accurate one by symbols.

decrease first, passing through a minimum, and then increase asymptotically towards constant values. A reverse trend is observed for the oscillation frequency, p_i. The parameters Ra_{TC}^{over}, A_C and p_i are seen to be independent of Pr when it becomes very large. Also, it is observed that the parameters Ra_{TC}^{over} and p_i decrease with increasing Le. The approximate approach (lines) is seen to agree well with the accurate one (symbols). For this case, the critical wavelength is always finite (multicellular flow). However, for Neumann boundary conditions ($a = 1$), the flow could be unicellular or multicellular at the onset of overstabilities, depending on the governing parameters.

According to the approximate approach, as shown in figure 4(*b*), for the value of Ra_S considered here, the flow is multicellular in a narrow range of Pr. The range is observed to decrease with increasing Le. Also, as can be seen from figure 4(*b*), Ra_{TC}^{over} is a monotonic function of Pr; however, the critical wavelength is infinity for higher and lower values of Pr for which the oscillatory frequency vanishes. On the other hand, the accurate approach predicted that the flow at the onset of overstabilities is always multicellular (finite wavelength) as shown in figure 4(*b*). Like the Dirichlet case, figure 4(*a*), the critical parameters for the Neumann case, figure 4(*b*), are found to be independent of Le when it becomes very large. For Neumann boundary conditions, the approximate approach is not reliable.

To be more confident about the present findings, the case of an infinite layer with $Ra_S = -10^5$, $Pr = 10$, $Le = 10^{1/2}$ and Neumann boundaries ($a = 1$) is considered. For this situation, the linear stability analysis predicted that $Ra_{TC}^{over} = 34\,047.6$, $A_C = 1.477$ and $p_i = 86.77$. By solving the full transient governing equations and using a unicellular flow as initial conditions with $Ra_T = 36\,000$, it was found that the flow is oscillatory and the single-cell flow pattern is broken into at least 13 convective cells travelling in the horizontal direction. The numerical results (not presented here) are obtained in a finite container having an aspect ratio of $A = 10$ to approximate the case of an infinite layer. It was found that the spatial period of the convective rolls is roughly 1.33–1.53 (13 to 15 cells, the number is varying in time while the cells travel horizontally) which compares well with the value of 1.48 at the onset of oscillatory convection for the case of an infinite layer.

4.2. *Finite-amplitude convection*

4.2.1. *Weak nonlinear theory*

Finite-amplitude convection, near the threshold of monotonic instabilities, is now investigated using the Galerkin method with a limited series representation. Assuming two-dimensional flows with the hypothesis that the convective rolls are rectangular and have their axes perpendicular to the vertical plane (x, z), analytical solutions will be derived for the Dirichlet and Neumann boundary conditions. For ideal hydrodynamic boundary conditions, it was demonstrated by Veronis (1968), Platten & Legros (1984) and Ahlers & Lücke (1987) that, in the vicinity of the onset of monotonic convection, the perturbation profiles can be developed in a limited Fourier series representation as

$$\left.\begin{aligned} \psi(t, x, z) &= \psi_0(t)\, F(x, z), \\ \theta(t, x, z) &= \theta_0(t)\, G(x, z) + \theta_1(t)\, h(x, z), \\ \phi(t, x, z) &= \phi_0(t)\, G(x, z) + \phi_1(t)\, h(x, z), \end{aligned}\right\} \tag{4.24}$$

where the amplitudes $\psi_0(t)$, $\theta_0(t)$, $\theta_1(t)$, $\phi_0(t)$ and $\phi_1(t)$ are time functions while $F(x, z)$, $G(x, z)$ and $h(x, z)$ are space functions describing the perturbation profiles in the vicinity of the onset of monotonic convection. These functions must satisfy the boundary conditions given by (2.4). According to Veronis (1968), Platten & Lagros (1984) and Ahlers & Lücke (1987), the functions $F(x, z)$ and $G(x, z)$ can be chosen to be the temperature and concentration perturbation profiles corresponding to the incipient flow and the function $h(x, z)$ as

$$\left.\begin{aligned} h(x, z) &= \sin(2\pi z) \quad \text{for } a = 0, \\ h(x, z) &= \sin(\pi z) \quad \text{for } a = 1. \end{aligned}\right\} \tag{4.25}$$

For the present problem, a similar approach will be used to study the stability

of the system with experimental boundary conditions. Since Fourier series are not suitable for this situation because of the non-slip boundary conditions, the functions $F(x,z)$ and $G(x,z)$ will be chosen to be those predicted numerically by the linear stability analysis described in the previous § 4.1.

Substituting (4.24) into (2.1) and using the functions $F(x,z)$, $G(x,z)$ and $h(x,z)$ as the weighted functions, the weak Galerkin formulation leads to the following set of ordinary differential equations:

$$\mathscr{M}_\psi \frac{\mathrm{d}\psi_0}{\mathrm{d}t} + \mathscr{K}_\psi \psi_0 = \mathscr{B}\left(Ra_T\theta_0 + \frac{Ra_S}{Le}\phi_0\right), \tag{4.26}$$

$$\left.\begin{aligned} \mathscr{M}\frac{\mathrm{d}\theta_0}{\mathrm{d}t} - \mathscr{L}\psi_0 + \mathscr{L}_1\psi_0\theta_1 &= -\mathscr{K}\theta_0, \\ \mathscr{M}_1\frac{\mathrm{d}\theta_1}{\mathrm{d}t} - \mathscr{L}_2\psi_0\theta_0 &= -\mathscr{K}_1\theta_1, \end{aligned}\right\} \tag{4.27}$$

$$\left.\begin{aligned} \mathscr{M}\frac{\mathrm{d}\phi_0}{\mathrm{d}t} - \mathscr{L}\psi_0 + \mathscr{L}_1\psi_0\phi_1 &= -\frac{\mathscr{K}}{Le}\phi_0, \\ \mathscr{M}_1\frac{\mathrm{d}\phi_1}{\mathrm{d}t} - \mathscr{L}_2\psi_0\phi_0 &= -\frac{\mathscr{K}_1}{Le}\phi_1, \end{aligned}\right\} \tag{4.28}$$

where the $\mathscr{B}$, $\mathscr{K}_\psi$, $\mathscr{K}$, $\mathscr{K}_1$, $\mathscr{L}$, $\mathscr{L}_1$, $\mathscr{L}_2$, $\mathscr{M}_\psi$, $\mathscr{M}$ and $\mathscr{M}_1$ are defined in (C 1). For a given set of the governing parameters, the ordinary differential equations, (4.26)–(4.28), can be solved numerically using, for example, the Runge–Kutta method. However, explicit steady-state solutions, when they exist, can be derived. For this situation, the solution in terms of ψ_0 is given by the following polynomial equation:

$$\psi_0(Le^4\psi_0^4 - 2b^2d_1Le^2\psi_0^2 - b^4d_2) = 0, \tag{4.29}$$

where d_1 and d_2 are given by

$$d_1 = Le^2(Ra_T^0 - 1) + Ra_S^0 - 1, \quad d_2 = 4Le^2(Ra_T^0 + Ra_S^0 - 1), \tag{4.30}$$

in which Ra_T^0 and Ra_S^0 are the normalized Rayleigh numbers and

$$Ra^{sup} = \frac{\mathscr{K}_\psi\mathscr{K}}{\mathscr{B}\mathscr{L}}, \quad b = \left(\frac{\mathscr{K}\mathscr{K}_1}{2\mathscr{L}_1\mathscr{L}_2}\right)^{1/2}. \tag{4.31}$$

In the present notation, similar equations have been derived by Da Costa *et al.* (1981) for the case with stress-free and Dirichlet boundary conditions.

Within the present approach, the parameter b is a constant which depends only on the aspect ratio of the enclosure and the boundary conditions. Some typical values of b are given in table 7 for various boundary conditions. The results are obtained with a grid size of 12×12 for a square cavity and 12×24 for an infinite horizontal layer. When the wavenumber is zero, an aspect ratio $A = 100$ is considered to simulate the infinite layer.

The only results available in the literature are those reported by Da Costa *et al.* (1981) for the case of a horizontal layer with ideal boundary conditions. For this situation, one can deduce from their analysis that $b = \sqrt{12}$ which agrees well with the present result ($b = 3.47$, see table 7 for $A = \infty$, $a = 0$ and stress-free boundary conditions (FF)). More results will be discussed in § 5.

	RR	RR	RR	RR	RF	RF	RF	RF	FF	FF	FF	FF
A	1	∞	1	∞	1	∞	1	∞	1	∞	1	∞
a	0	0	1	1	0	0	1	1	0	0	1	1
b	2.99	2.72	1.63	1.61	3.10	3.10	1.56	1.53	3.13	3.47	1.48	1.41

TABLE 7. Computed values of b for a square enclosure and infinite horizontal layer for different boundary conditions.

4.2.2. *Asymptotic analytical solution*

To support our present analysis, an accurate analytical solution will be developed for finite-amplitude convection for the case of a shallow ($A \gg 1$) enclosure, subject to constant fluxes of heat and solute ($a = 1$), using the parallel flow concept. In the past, this concept has been used with success by many authors such as Cormack, Leal & Imberger (1974) and Mamou, Vasseur & Bilgen (1996, 1998) to predict the flow behaviour. For a shallow enclosure, it may be assumed that the flow in the central part of the enclosure is parallel such that the stream function depends only on z. Thus we can write $\psi(x,z) \simeq \psi(z)$. Also, it can be easily demonstrated that the temperature and concentration fields can be decomposed as $\theta(x,z) = C_T x + f_T(z)$ and $\phi(x,z) = C_S x + f_S(z)$, where C_T and C_S are the horizontal gradients of temperature and concentration, respectively, and f_T and f_S are unknown functions. Using the above approximations, the steady solution of the governing equations, (2.1), yields

$$\left.\begin{aligned} \psi(x,z) &= \psi_0(16z^4 - 8z^2 + 1), \\ \theta(x,z) &= C_T x + \frac{C_T \psi_0}{15}(48z^5 - 40z^3 + 15z), \\ \phi(x,z) &= C_S x + \frac{LeC_S \psi_0}{15}(48z^5 - 40z^3 + 15z), \end{aligned}\right\} \tag{4.32}$$

where ψ_0 is the stream function value at the centre of the enclosure defined as

$$\psi_0 = \frac{15}{8}\left(Ra_T^0 C_T + \frac{Ra_S^0}{Le} C_S\right), \tag{4.33}$$

in which $Ra_T^0 = Ra_T / Ra^{sup}$ and $Ra_S^0 = Ra_S / Ra^{sup}$ with $Ra^{sup} = 720$.

Performing the energy and solute balances at any vertical section of the enclosure, it is readily found that

$$C_T = \frac{16b^2\psi_0}{15(2b^2 + \psi_0^2)} \quad \text{and} \quad C_S = \frac{16b^2 Le\psi_0}{15(2b^2 + Le^2\psi_0^2)}, \tag{4.34}$$

where $b = (315/256)^{1/2}$.

Substituting (4.34) into (4.33), yields

$$\psi_0(Le^4\psi_0^4 - 2b^2 d_1 Le^2\psi_0^2 - b^4 d_2) = 0, \tag{4.35}$$

where d_1 and d_2 are given by (4.30). The above polynomial equation is similar to (4.29).

The local heat and mass transfer rates are uniform and they are defined, according to (2.6) and (2.7), by

$$Nu = \frac{10}{3}\left(\frac{\psi_0^2 + 2b^2}{\psi_0^2 + 20b^2/3}\right) \quad \text{and} \quad Sh = \frac{10}{3}\left(\frac{Le^2\psi_0^2 + 2b^2}{Le^2\psi_0^2 + 20b^2/3}\right). \tag{4.36}$$

To validate the parallel flow concept, some numerical data, obtained by solving the full governing equations (2.1), are compared to the analytical solution. The results are illustrated in figure 5 for $Ra_T^0 = 3$, $Ra_S^0 = -2$, $Le = 10$, $Pr = 7$, $A = 10$, $a = 1$ and rigid boundaries. Figure 5(a) demonstrates clearly the parallel flow characteristics such as the parallelism of the streamlines with respect to the horizontal walls (except at the end regions) and the horizontal linear variations of temperature and concentration. Figures 5(b) and 5(c) illustrate a comparison between the numerical (symbols) and analytical (solid lines) solutions in terms of mid-height horizontal profiles of ψ, T and S. In figures 5(d) and 5(e) mid-width vertical profiles are also shown. As can be observed, good agreement is obtained between the two types of solutions in the central part of the enclosure ($-4 \leqslant x \leqslant 4$). It is noted that the present results are obtained exactly at the threshold of monotonic instability, ($Ra_{TC}^{sup} = 3 \times Ra^{sup}$). This convective flow is due to the fact that the stabilizing agent (solute) is the slower diffusing component ($Le = 10$). For this situation, the nonlinear advective terms in the solute conservation equation distort considerably the linear concentration field and the solute gradient in the bulk of the layer is reduced, as shown in figures 5(a) and 5(c). Therefore, the thermal gradient in that region becomes dominant and gives rise to the convective flow. The imposition of a constant heat flux, without altering the imposed mass flux, increases the fluid amplitude velocity and the solute transfer is thus enhanced. As a result, a large amount of solute is removed from the hot wall and transported by convection to the cold wall. This mechanism leads to a solute deficit near the lower boundary and a surplus near the upper one. To compensate for the solute deficit and adjust the surplus, a downward solute transfer appears in the bulk of the enclosure and gives rise to an adverse solute gradient (see the vertical concentration profiles in figure 5e) that contributes to the destabilization of the system. As a result, convective flows are made possible beneath the threshold of monotonic instabilities.

4.2.3. *Stability analysis of the asymptotic solution: accurate approach*

In this section, the stability of the parallel flow solution is studied and the critical Rayleigh number for Hopf bifurcation is determined. The total solution including the perturbations can be written as follows:

$$\left.\begin{aligned} \psi(x,z,t) &= \psi_b(x,z) + \psi_p(x,z,t), \\ \theta(x,z,t) &= \theta_b(x,z) + \theta_p(x,z,t), \\ \phi(x,z,t) &= \phi_b(x,z) + \phi_p(x,z,t), \end{aligned}\right\} \tag{4.37}$$

where ψ_b, θ_b and ϕ_b represent the basic fully developed solution (4.32) and ψ_p, θ_p and ϕ_p are the perturbation profiles which can be represented by (4.10). The linear problem, after neglecting the small quantities, is obtained as follows:

$$\left.\begin{aligned} &p\left(-\omega^2 F + \frac{\mathrm{d}^2F}{\mathrm{d}z^2}\right) - \mathrm{i}\omega\left[\left(\frac{\mathrm{d}^3\psi_b}{\mathrm{d}z^3} + \omega^2\frac{\mathrm{d}\psi_b}{\mathrm{d}z}\right)F - \frac{\mathrm{d}\psi_b}{\mathrm{d}z}\frac{\mathrm{d}^2F}{\mathrm{d}z^2}\right] \\ &\qquad = Pr\left(\omega^4 F - 2\omega^2\frac{\mathrm{d}^2F}{\mathrm{d}z^2} + \frac{\mathrm{d}^4F}{\mathrm{d}z^4}\right) - \mathrm{i}\omega Pr\left(Ra_T G + \frac{Ra_S}{Le}H\right), \\ &p\,G + \mathrm{i}\omega\left(1 - \frac{\mathrm{d}\theta_b}{\mathrm{d}z}\right)F + C_T\frac{\mathrm{d}F}{\mathrm{d}z} - \mathrm{i}\omega\frac{\mathrm{d}\psi_b}{\mathrm{d}z}G = -\omega^2 G + \frac{\mathrm{d}^2G}{\mathrm{d}z^2}, \\ &p\,H + \mathrm{i}\omega\left(1 - \frac{\mathrm{d}\phi_b}{\mathrm{d}z}\right)F + C_S\frac{\mathrm{d}F}{\mathrm{d}z} - \mathrm{i}\omega\frac{\mathrm{d}\psi_b}{\mathrm{d}z}H = \frac{1}{Le}\left(-\omega^2 H + \frac{\mathrm{d}^2H}{\mathrm{d}z^2}\right). \end{aligned}\right\} \tag{4.38}$$

The finite element method is used to solve the above linear eigenvalue problem. The resulting system of linear equations is similar to that given in (4.23). The elementary matrices are given in Appendix D.

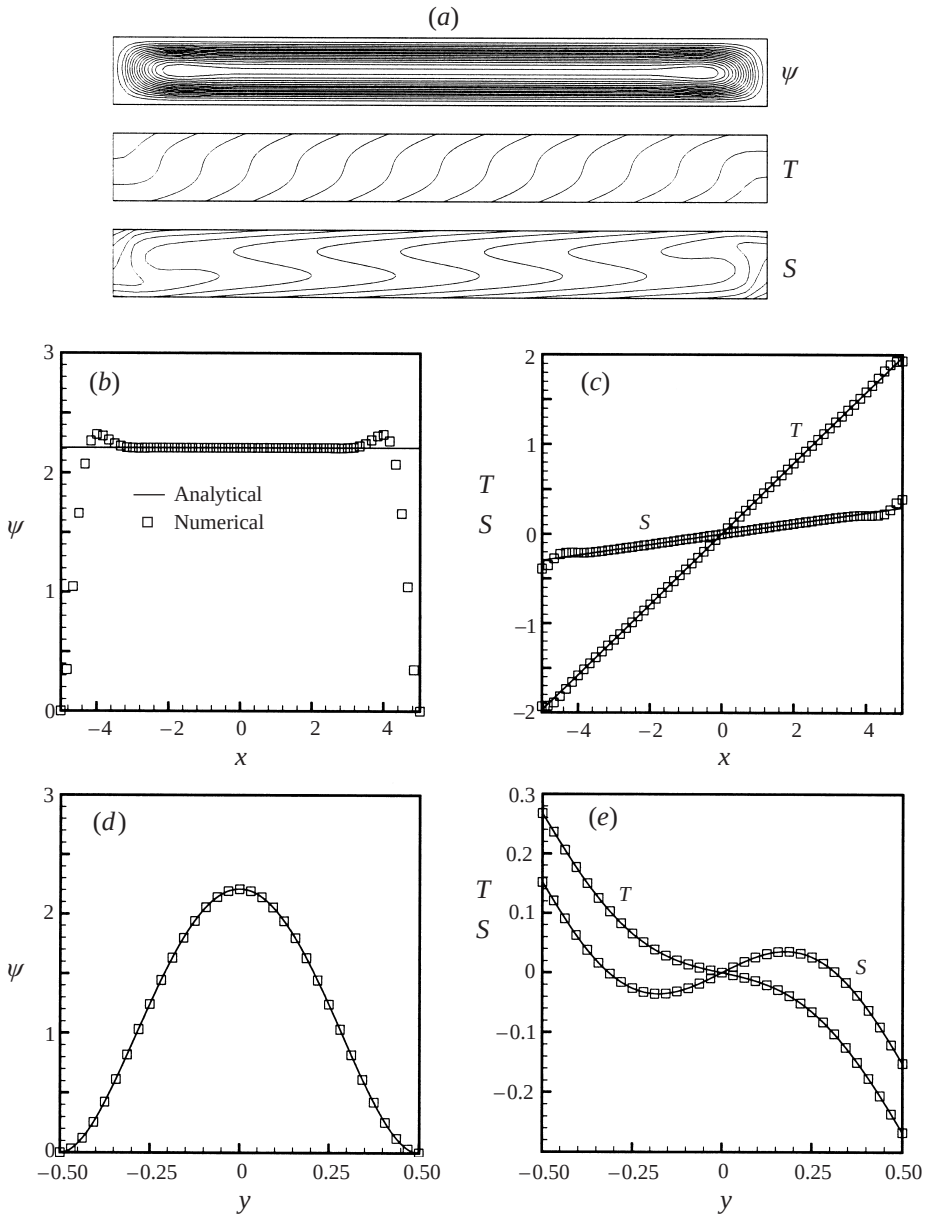

FIGURE 5. Comparison between the numerical results and the analytical parallel flow solution for $Ra_T^0 = 3$, $Ra_S^0 = -2$, $Pr = 7$, $Le = 10$, $A = 10$, $a = 1$ and rigid boundaries ($Ra^{sup} = 722.57$): (*a*) streamlines, isotherms and isoconcentrations, (*b*) horizontal stream function profile at the mid-height of the enclosure, (*c*) horizontal temperature and concentration profiles at the mid-height of the enclosure, (*d*) vertical stream function profile at the mid-width of the enclosure, (*e*) vertical temperature and concentration profiles at the mid-width of the enclosure. Numerical solution: $\psi_0 = 2.2084$, $\psi_{max} = 2.3199$, $Nu_{x=0} = 1.8697$, $Nu_m = 1.8051$, $Sh_{x=0} = 3.3188$ and $Sh_m = 3.3633$. Analytical solution: $\psi_0 = 2.2086$, $Nu_{x=0} = Nu_m = 1.8701$ and $Sh_{x=0} = Sh_m = 3.2947$.

The present numerical procedure is validated with the results of Kimura, Vynnycky & Alavyoon (1995) obtained for a Darcy porous medium in thermal convection. To simulate their case with the present governing equations, (2.1), the Prandtl number is made very large ($Pr \sim 10^6$) in order to neglect the inertial term, which is the case in a porous medium. The viscous term in the governing equations, $\nabla^4\psi$, is replaced by $-\nabla^2\psi$ and the solutal buoyancy force is cancelled ($Ra_S = 0$). To obtain the threshold for Hopf bifurcation (transition from steady to oscillatory convection) the critical Rayleigh number and wavelength are obtained in the same manner as described in § 4.1.4. Using 30 finite elements in the vertical direction, the critical Darcy Rayleigh number for Hopf bifurcation is obtained as $R_{TC}^{hopf} = 506.069$, the corresponding critical wavelength is $A_C = 1.3023$ and the oscillation frequency is obtained as $p_i = 138.906$. These results are seen to agree well with those obtained by Kimura *et al.* (1995).

For double-diffusive convection, the basic solution is obtained as a function of the governing parameters, namely Ra_T, Ra_S and Le. For $Ra_S = -2 \times Ra^{sup}$, $Pr = 7$, $Le = 10$ and $a = 1$, the critical Rayleigh number which characterizes the transition from steady to oscillatory flow (Hopf bifurcation) is obtained as $Ra_{TC}^{hopf} = 52\,028.9$, the corresponding critical wavelength is $A_C = 1.579$ and the oscillation frequency is $p_i = 135.27$. For this situation, the perturbation profiles for the stream function, temperature and solute, are illustrated in figure 6. For an enclosure having an aspect ratio $A = 10$, the numerical results of the fully governing equations indicate that the transition from steady to oscillatory convection occurs within the range of the Rayleigh number $52\,000 < Ra_T < 55\,000$, which is in agreement with the linear stability analysis prediction. Near the threshold of oscillatory convection, the amplitude of the oscillation is very small and changes in the flow structure are not noticeable. To clearly illustrate the unsteadiness of the flow structure, a relatively high Rayleigh number of $Ra_T = 70\,000$ is considered. For this value, according to the linear stability analysis, as shown in figure 7, the parallel flow solution is unstable to perturbations of wavelength $0.92 \leqslant A \leqslant 2.64$. The growth rate parameter p is computed for fixed values of Ra_T, Ra_S, Le and Pr by varying the wavelength A. In this range ($0.92 \leqslant A \leqslant 2.64$), it was found that there are at least two eigenvalues with positive real parts. The one with a maximum value and the corresponding oscillation frequency are illustrated in figure 7(a) as functions of the wavelength A. The dominating perturbation is the one that has a maximum real part of the growth rate parameter, p_r. As shown in figure 7(a), the maximum value is obtained for $A = 1.32$ and the corresponding oscillatory frequency is $p_i = 185.68$. For $Ra_T = 70\,000$, the oscillatory behaviour of the nonlinear convective solution is depicted in figures 7(b) and 7(c), for an aspect ratio of $A = 10$, in terms of the time history of the flow intensity, ψ_0, and the flow structure time-evolution, respectively. The oscillation period is $\tau = 0.0335$ ($p_i = 2\pi/\tau = 187.56$). Since the oscillation amplitude is weak, the linear and nonlinear predictions were found to agree well. The small discrepancy between these two approaches is probably attributable to the fact that the numerical results are obtained with a finite aspect ratio. From figure 7(c), it is observed that the main flow remains unicellular but the parallel flow loses its characteristics and the oscillatory behaviour is exemplified by the presence of a series of small secondary vortices at the mid-height of the enclosure. These vortices are born at the centre of the enclosure, from where, they are seen to travel to the left and to the right vertical boundaries where they collapse.

For pure thermal convection ($Ra_S = 0$), the critical Rayleigh number, the critical wavelength and the corresponding oscillatory frequency for Hopf bifurcation are given respectively by $Ra_{TC}^{hopf} = 51\,854.4$, $A_C = 1.579$ and $p_i = 135.28$.

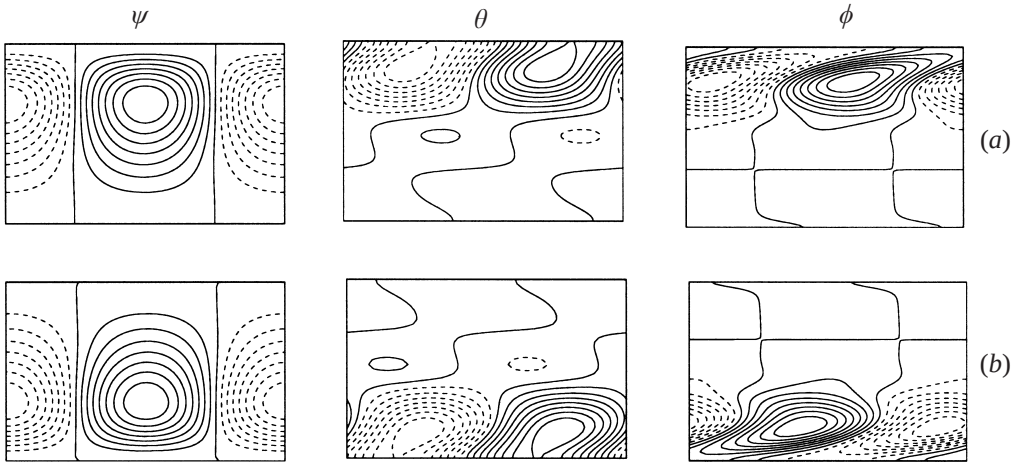

FIGURE 6. Perturbation profiles at the threshold for Hopf bifurcation for $Ra_S = -2Ra^{sup}$, $Pr = 7$, $Le = 10$ and $a = 1$ in an infinite layer with rigid boundaries: (*a*) $p_i = 135.27$ and (*b*) $p_i = -135.27$.

5. Results and discussion

In this section, a comparison is made between the predictions of the linear and nonlinear theories and the numerical solution of the full governing equations.

From the analytical nonlinear theory results, (4.29) and (4.35), it is easily found that the solution for ψ_0 is

$$\psi_0 = 0, \tag{5.1}$$

and

$$\psi_0 = \pm\frac{b}{Le}\left(d_1 \pm \sqrt{d_1^2 + d_2}\right)^{1/2}. \tag{5.2}$$

The above equations indicate that five different steady-state solutions are possible. One corresponds to the purely diffusive regime ($\psi_0 = 0$) and the four others to convective flow regimes. The signs + and − outside the brackets refer to counter-clockwise and clockwise circulation, respectively. Within the brackets, they refer to convective stable and unstable solutions, respectively. The stability analysis of these two solutions will be discussed later. Also, it is observed from (5.2) that two types of bifurcation are possible. The first one, called hereafter supercritical bifurcation, is characterized by the fact that the transition from the quiescent state to the convective regime occurs through zero flow amplitude ($\psi_0 = 0$). The threshold, expressed in terms of the supercritical Rayleigh number Ra_{TC}^{sup}, is obtained, when the conditions $d_1 < 0$ and $d_2 = 0$ are satisfied, as

$$Ra_{TC}^{sup} = (1 - Ra_S^0)Ra^{sup}, \tag{5.3}$$

which is similar to the results predicted by the linear stability analysis, (4.17).

The second one, called subcritical bifurcation, is characterized by the fact that the onset of motion occurs through finite-amplitude convection ($\psi_0 = \pm b\sqrt{d_1}/Le$). As discussed by Veronis (1968), subcritical convection is possible only when the two buoyancy forces are opposing each other ($Ra_T > 0$ and $Ra_S < 0$ or vice versa) and when the stabilizing agent is the slower diffusing component. In the present analysis, it can be demonstrated, from the nonlinear theories, that subcritical flows occur when

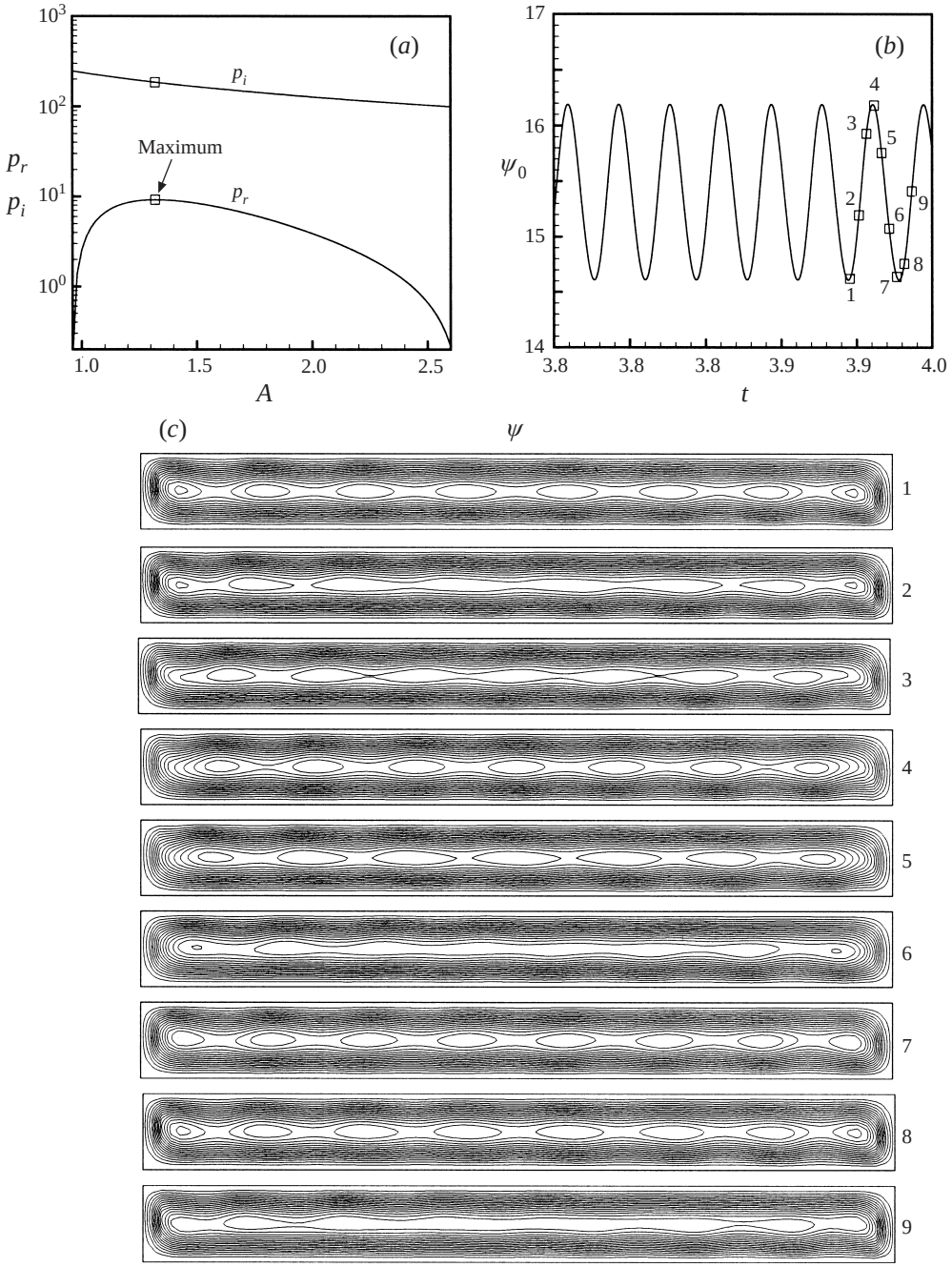

FIGURE 7. (*a*) Perturbation growth rate p_r and p_i as functions of the wavelength A. (*b*) Time history of the flow intensity ψ_0 and (*c*) time-evolution of the flow structure, for $Ra_T = 70\,000$, $Ra_S = -2 \times Ra^{sup}$, $Pr = 7$, $Le = 10$ and $a = 1$ with rigid boundaries.

$Ra_S < 0$ and $Le > 1$ and more precisely when

$$Ra_S < 0 \quad \text{and} \quad Le > \sqrt{\frac{Ra_S^0 - 1}{Ra_S^0}}. \tag{5.4}$$

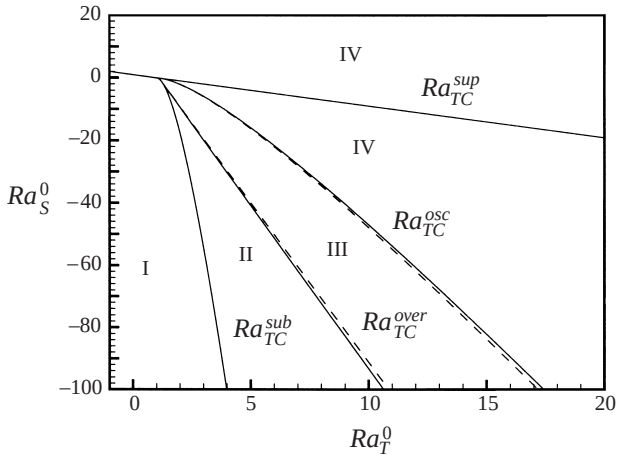

FIGURE 8. Stability diagram for a square enclosure with rigid boundaries, $Pr = 7$ and $Le = 10$ with $a = 0$ and 1. The results obtained with Dirichlet boundary conditions ($a = 0$) are shown with solid lines and those with Neumann boundary conditions ($a = 1$) with dashed lines.

These flows are initiated at a threshold, corresponding to a saddle-node point, called the subcritical Rayleigh number Ra_{TC}^{sub}, which can be obtained from the conditions $d_1 > 0$ and $d_1^2 + d_2 = 0$, as

$$Ra_{TC}^{sub} = Le^{-2}\left(\sqrt{Le^2 - 1} + \sqrt{-Ra_S^0}\right)^2 Ra^{sup}. \tag{5.5}$$

A similar expression for the case of an infinite horizontal layer with ideal boundary conditions has been derived by Veronis (1968) when considering Dirichlet boundary conditions ($a = 0$) for which $Ra^{sup} = 27\pi^4/4$.

The regions delineating the different regimes described in the above section will now be discussed on the basis of the linear and nonlinear theories. Typical results, for the case of a square enclosure, are illustrated in figure 8 for $Pr = 7$ and $Le = 10$. The four critical Rayleigh numbers, Ra_{TC}^{sub}, Ra_{TC}^{over}, Ra_{TC}^{osc} and Ra_{TC}^{sup}, are presented in the plane Ra_T^0, Ra_S^0. Four distinct regions are delineated. The first one, denoted by I, corresponds to the diffusive regime ($Ra_T < Ra_{TC}^{sub}$). Both linear and nonlinear theories indicate that the system is stable such that any dynamic perturbation will decay to the rest state situation. The second region, denoted by II ($Ra_{TC}^{sub} < Ra_T < Ra_{TC}^{over}$), refers to the subcritical convective regime. According to the linear theory, the rest state is stable to an infinitesimal disturbance. However, the nonlinear one predicts that the diffusive regime can be disturbed by a large finite-amplitude dynamic perturbation. The third region III ($Ra_{TC}^{over} < Ra_T < Ra_{TC}^{osc}$), describes the overstable regime in which any dynamic perturbation will evolve in an oscillatory manner from the rest state. In that region, oscillatory and steady convective modes are possible. The region IV delineated by $Ra_T > Ra_{TC}^{osc}$ corresponds to the direct monotonic convective regime.

Bifurcation diagrams for the steady-state solution are presented in figures 9 and 10 for different values of the solutal Rayleigh and Lewis numbers. The flow amplitude, ψ_0, is normalized with respect to the constant b, ($\psi_n = \psi_0/b$), and the thermal and solutal Rayleigh numbers are normalized with respect to the critical parameter Ra^{sup}. The resulting diagrams are thus independent of the aspect ratio of the enclosure and the hydrodynamic, thermal and solutal boundary conditions considered in this study.

The results corresponding to the case of opposing flows, in which the solute is

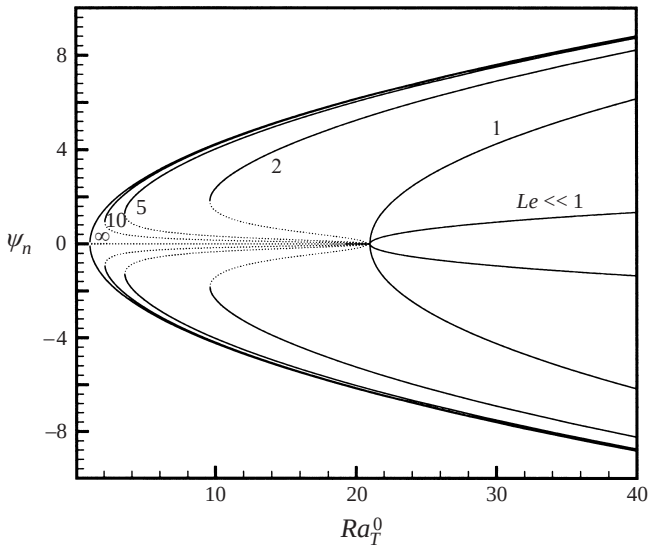

FIGURE 9. Bifurcation diagram for opposing steady flows when $Ra_S^0 = -20$: normalized flow intensity, $\psi_n = \psi_0/b$, versus Ra_T^0 for different Lewis numbers.

stabilizing ($Ra_S^0 < 0$), are depicted in figure 9 for $Ra_S^0 = -20$. For this situation, both subcritical and oscillatory flows are possible as predicted by the present theories. As already discussed while considering the nonlinear theory results, there exists two types of bifurcation, one supercritical and the other one subcritical. For the first type, convection sets in at a Rayleigh number $Ra_T = Ra_{TC}^{sup} = 21 \times Ra^{sup}$. For subcritical bifurcation, convective flow sets in at a Rayleigh number $Ra_T = Ra_{TC}^{sub}$ well below the threshold of monotonic instability ($Ra_{TC}^{sub} < Ra_{TC}^{sup}$). The linear theory, on the other hand, predicts that steady and oscillatory flows are possible below the supercritical Rayleigh number, when the stabilizing agent (solute) is the slower diffusing component ($Le > 1$). The threshold for such flows is characterized by the overstable critical Rayleigh number, Ra_{TC}^{over}. For the value $Ra_S^0 = -20$ considered here, the Lewis number that characterizes the transition between the supercritical and subcritical bifurcations is $Le_t = (21/20)^{1/2} \simeq 1.025$, (5.4). Thus, as can be observed from figure 9, the bifurcation is supercritical when $Le < Le_t$ and subcritical when $Le > Le_t$. The solutions depicted by solid lines, referred to as stable branches, are expected to be stable. Those with dotted lines, referred to as unstable branches, are seen to vanish above the supercritical threshold. They are believed to be unstable since the linear theory predicts that any infinitesimal perturbation grows with time near the threshold of supercritical convection. In the subcritical regime, the transition from the rest state to the convective mode occurs through finite-amplitude convection. As a result, the flow amplitude velocity is finite at the threshold from where the stable and unstable branches bifurcate. As the Lewis number is increased, the subcritical value of the flow amplitude (ψ_0^{sub}; the value of ψ_0 at $Ra_T = Ra_{TC}^{sub}$) is seen to increase first and then decreases towards zero as $Le \to \infty$.

Some typical analytical and numerical results are presented in figure 10 for $Ra_S^0 = -2$, $Pr = 7$, $Le = 10$ and $a = 0$ and 1, in terms of the flow amplitude ψ_0 as function of the thermal Rayleigh number, Ra_T^0. Figure 10(a) corresponds to the case of a square enclosure and figure 10(b) to an infinite horizontal layer. The numerical results are represented by symbols. The four critical Rayleigh numbers are given in table 8.

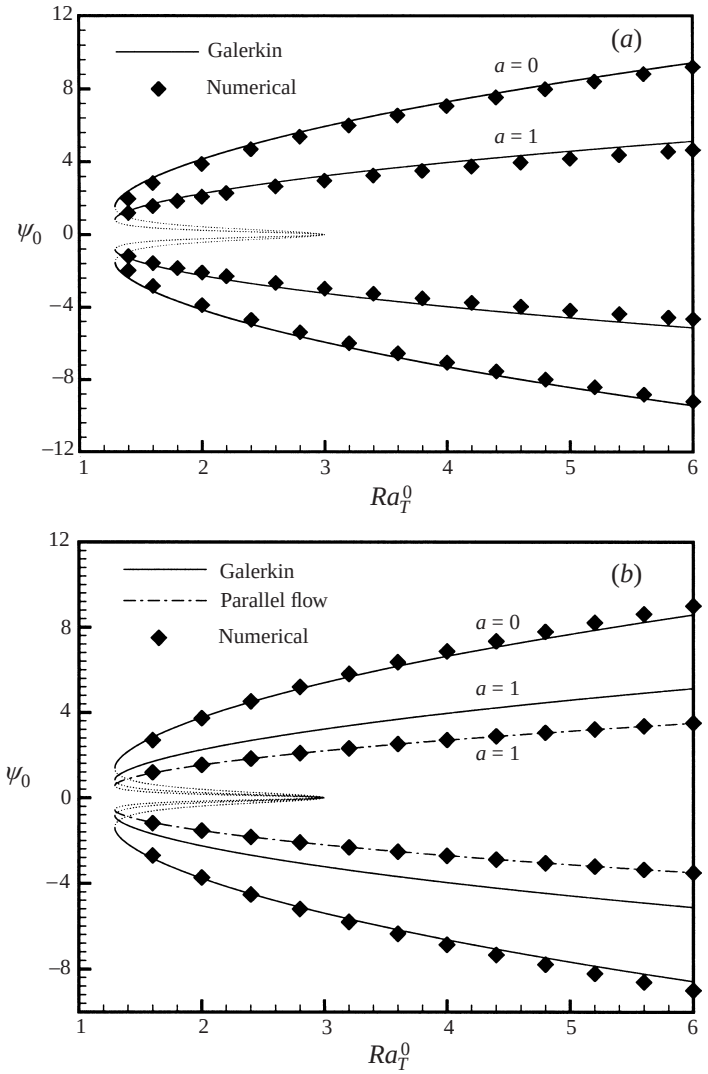

FIGURE 10. Bifurcation diagram for opposing steady flows for $Ra_S^0 = -2$, $Pr = 7$, $Le = 10$, $a = 0$ and 1 and rigid boundaries: flow intensity, ψ_0, versus Ra_T^0: (*a*) square enclosure, (*b*) infinite horizontal layer ($A = 2$).

For a square enclosure ($A = 1$), the nonlinear analytical results are seen to agree well with the numerical ones. By decreasing Ra_T^0 from 6 to 1 step by step, using the previous solution as initial conditions, the steady-state solution is observed to persist down to $Ra_T^0 \simeq 1.4$. Below that value, the flow was found to oscillate periodically and to decay towards the rest state when Ra_T^0 is decreased below 1.29. However, using the rest-state solution as initial conditions, convective flows were found to appear just above the threshold of overstability, Ra_{TC}^{over}. In the vicinity of $Ra_T = Ra_{TC}^{over}$, the numerical results lead to permanently oscillating solutions and the steady branch cannot be reached. Increasing Ra_T^0 progressively, the flow amplitude increases and the oscillation frequency is observed to decrease and vanish completely above $Ra_T^0 \simeq 1.45$ (for $a = 0$) and then the steady branch is reached. In the overstable regime, as

A	a	Ra^{sup}	Ra_{TC}^{sub}/Ra^{sup}	Ra_{TC}^{over}/Ra^{sup}	Ra_{TC}^{osc}/Ra^{sup}	Ra_{TC}^{sup}/Ra^{sup}
1	0	2585.04	1.2914	1.2967	1.9711	3
1	1	1684.53	1.2914	1.2982	1.9603	3
∞	0	1707.76	1.2914	1.3008	1.9785	3
∞	1	720.00	1.2914	1.3000	1.9485	3

TABLE 8. Critical Rayleigh numbers for $Ra_S^0 = -2$, $Pr = 7$, $Le = 10$, $A = 1$ and ∞, $a = 0$ and 1 and rigid boundaries.

demonstrated numerically, multiple confined states are possible. For instance, for $Ra_T^0 = 1.4$ and $a = 0$, two different solutions are possible. The first one depicted in figure 11(a) is steady and the second one in figure 11(b–d), is periodically oscillating. The two solutions are obtained by using finite-amplitude convection and the rest-state solution as initial conditions, respectively. Figures 11(b) and 11(c) illustrate the time history of the flow intensity extremum, ψ_{ext}, and of the Nusselt and Sherwood numbers, Nu_m and Sh_m. It can be observed from figure 11(c) that the heat and solute transfer rates are out of phase. At $t = 0$, figure 11(d) shows that the flow is counterclockwise and monocellular and the heat and solute transfer rates are almost maximum and minimum, respectively (figure 11c), such that the flow is dominated at this time by the thermal buoyancy force. As the time is increased, a stabilizing solute gradient is established progressively and the flow intensity decreases accordingly towards the rest state. As t reaches 0.2754, the flow intensity is weak and the flow patterns start to restructure, giving rise to the appearance of two clockwise small vortices in the vicinity of the top left and the bottom right corners of the enclosure. These two eddies grow and progressively squeeze the main flow cell as can be observed at $t = 0.3428$, 0.3442 and 0.3458 in figure 11(d). At $t = 0.3702$, a complete reversal of the flow circulation is obtained and then the flow intensity increases until $t = 0.5618$. This completes one half-period of the flow evolution. A symmetrical evolution process is repeated for the remaining half-period (see the flow structures in figure 11(d) for $t = 0.8372$ to 0.9320).

It is noted that, upon starting the numerical code with the rest-state solution as initial conditions with a grid size of 20×20 and $\Delta t = 5 \times 10^{-4}$, the flow intensity was found to increase in an oscillatory manner. At the beginning of convection ($|\psi_{ext}| \ll 1$), the sense of the flow circulation reverses cyclically with a time period $\tau = 0.791$. The transition from clockwise to counterclockwise circulation (or vice versa) occurs with the presence of multicellular flows as discussed for figure 11(d). For this case, it was found, according to the linear stability analysis, that $\gamma = 20.567$ and $\sigma = 2.624$ and the solution to the dispersion relationship, (4.14), consists of one real root ($p = -402.34$) and two complex-conjugate roots ($p = 0.992 \pm \mathrm{i}7.909$). Hence, the time period of oscillation is $\tau = 2\pi/7.909 = 0.794$ which is in good agreement with the value $\tau = 0.791$ predicted by the numerical code at the earlier stages of convection. When the flow achieves the permanently oscillating state (see figure 11b–d), the time period of the nonlinear oscillations increases to $\tau = 1.124$ due to the nonlinear effects.

As discussed above, the oscillatory flows in a square enclosure are characterized by a transition from a clockwise to a counterclockwise circulation and vice versa. The reversal of flow circulation occurs with the appearance of multicellular structures. For a shallow enclosure, the mechanism of the oscillatory flows is different. To illustrate this point, the above problem has been reconsidered for the case of rectangular enclosure of relatively large aspect ratio ($A = 5$). For this situation, according to the linear stability analysis, $Ra^{sup} = 1778.75$. Typical results for the oscillatory solution

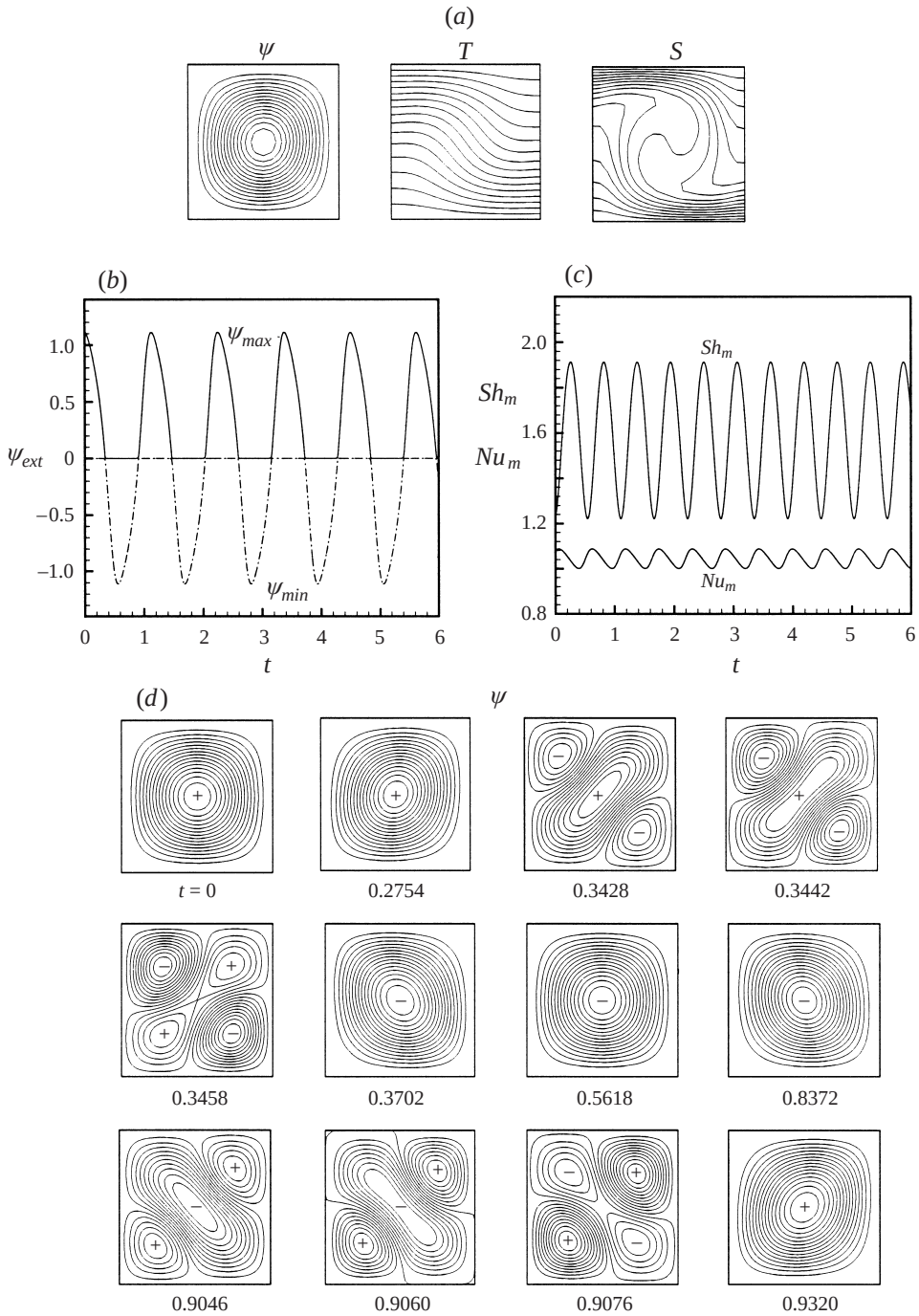

FIGURE 11. Steady and oscillatory flows for $Ra_T^0 = 1.4$, $Ra_S^0 = -2$, $Pr = 7$, $Le = 10$, $A = 1$, $a = 0$ and rigid boundaries. (*a*) Steady flows: $\psi_0 = 1.970$, $Nu_m = 1.253$ and $Sh_m = 3.009$, oscillatory flows. (*b*) Time history of the flow intensity ψ_{ext}. (*c*) Time history of the average heat and solute transfer rates Nu_m and Sh_m. (*d*) Time evolution of the flow structure. The sign + corresponds to counterclockwise rotation and − to clockwise.

are illustrated in figure 12, in terms of the time history of Nu_m and Sh_m (figure 12*a*) and streamlines, isotherms and isosolutes, at different time steps (figure 12*b–d*). The numerical results, obtained with a grid size of 12×50 and $\Delta t = 5 \times 10^{-4}$, indicate a periodic asymmetric oscillating flow consisting of five to six rolls travelling in the horizontal direction from left to right.

The travelling wave mechanism could be explained in the following manner. First it is known that, in horizontal enclosures subject to vertical gradients of heat and solute, either left or right travelling waves are possible. Hence, the final converged state depends considerably on initial convective flow conditions. Secondly, since the enclosure is bounded by four rigid and impermeable walls, the travelling waves occur with zero net flow in the horizontal. The present results are obtained by using a five-cell perturbation as initial conditions. As discussed above, the cells are observed to travel from left to right. The birth of the cells takes place near the left side of the cavity and disappear at the right lateral wall. Near the left vertical wall, where the viscous effects are dominant, the fluid is almost at rest. According to the linear stability analysis, this region is unstable and since the heat is the faster diffusing component, convective flow is generated before the mass flux is established. A convective cell starts to build up and then occupies the region. As time increases, the cell intensity becomes stronger and due to the presence of the lateral boundary, its centre of rotation is shifted to the right, pushing the other cells forward. To accommodate the newly arrived cell, the one at the other end of the cavity is squeezed and forced to collapse against the right lateral wall. A similar process is repeated each time a new cell appears. This mechanism leads to the forward displacement of the other cells. By examining the isotherms and isoconcentrations (figure 12*b–d*), one can observe that the downward and upward thermal and solutal plumes drift to the right and are tilted to the left from the vertical as if they had been pulled from their bases. The vorticity strength produced by the buoyancy forces is important in the plumes. Since these plumes are tilted, each convective roll experiences a negative and positive vorticity from one vertical side. This, since the flow circulation sense is controlled by the vorticity production, cause the convective rolls to move in the horizontal direction.

Since the aspect ratio is not large enough the cell velocity is not uniform and the oscillation amplitudes of the Nusselt and Sherwood numbers remain significant (see figure 12*a*). As will be discussed later, by increasing considerably the enclosure aspect ratio, the cell velocity becomes uniform and the oscillation amplitudes dwindle leading to time-independent heat and mass overall transfer rates.

Now the case of an infinite layer is investigated for the same set of governing parameters and the results are presented in figure 10(*b*). Periodic boundary conditions and an aspect ratio of $A = A_C = 2$ are considered to simulate the flow when the horizontal boundaries are maintained at constant temperature and concentration. When these boundaries are subject to constant fluxes of heat and solute, an enclosure of aspect ratio $A = 10$ with rigid boundaries is considered for the numerical results. For $a = 0$, the numerical results indicate that, in the overstable regime $Ra_{TC}^{over} \leqslant Ra_T \leqslant Ra_{TC}^{osc}$, both standing and travelling wave solutions are possible. For instance, for $Ra_T^0 = 1.4$, a standing wave solution is obtained (see figure 13*a*) upon using finite-amplitude convection as initial conditions. However, using the rest state as initial conditions,

FIGURE 12. Oscillatory flows for a shallow enclosure, $Ra_T^0 = 1.4$, $Ra_S^0 = -2$, $Pr = 7$, $Le = 10$, $A = 5$ and $a = 0$: (*a*) time history of the Nusselt number, Nu_m, and Sherwood number, Sh_m; (*b-d*) time evolution of the flow patterns, temperature and concentration fields.

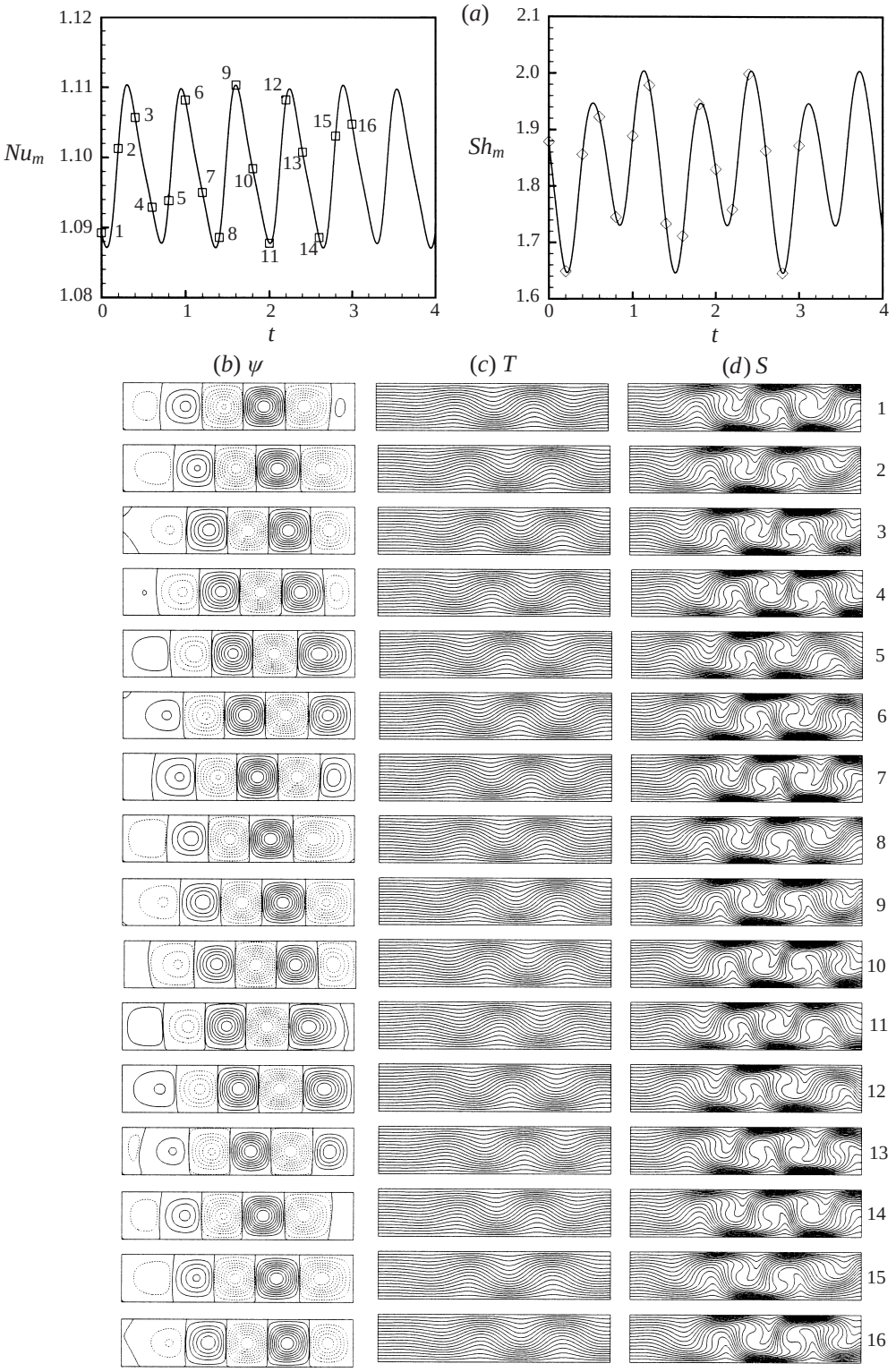

FIGURE 12. For caption see facing page.

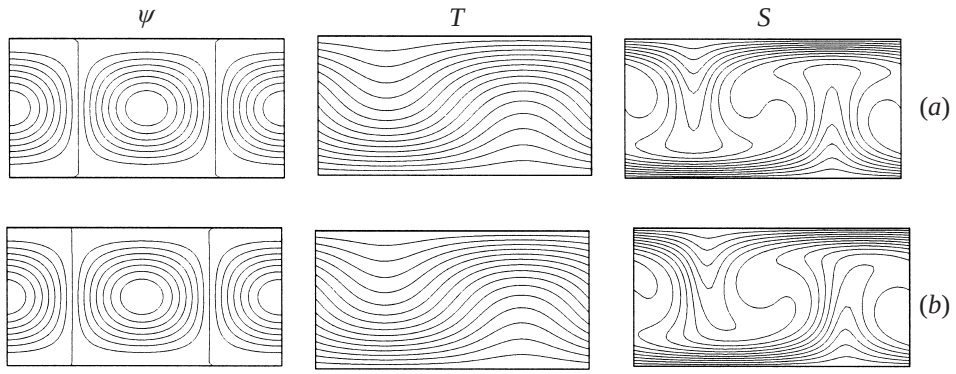

FIGURE 13. Standing and travelling waves in an infinite horizontal layer for $Ra_T^0 = 1.4$, $Ra_S^0 = -2$, $Pr = 7$, $Le = 10$, $A = A_C = 2$ and $a = 0$: (*a*) standing wave: $\psi_{max} = -\psi_{min} = 1.898$, $Nu_m = 1.280$ and $Sh_m = 3.197$; (*b*) left travelling wave at constant velocity $u_C = 0.634$, $\psi_{max} = -\psi_{min} = 1.910$, $Nu_m = 1.282$ and $Sh_m = 3.018$.

the oscillatory behaviour of the flow is transformed into a left travelling wave with constant velocity $u_c = 0.634$ (see figure 13*b*). For the standing wave, the thermal and solutal plumes are vertical as can be observed from figure 13(*a*). Naturally, for the travelling wave solution, the plumes are tilted to the right from the vertical. Similar phenomena have been observed by Deane *et al.* (1987) while considering stress-free horizontal boundaries. As discussed by these authors, standing, travelling, modulated and chaotic waves are possible. By increasing Ra_T^0, the oscillation frequency or the horizontal velocity are found to decrease towards zero and then the solution bifurcates towards the stable branch.

The stability of the analytical solutions is briefly discussed here. As discussed in the beginning of this section, below the threshold for stationary convection two convective branch solutions are possible. The one with low flow intensity is believed to be unstable. Within the range of the governing parameters considered in this study, according to the numerical solution of the full governing equations, it is found that the lower solution is unstable and could not be sustained. The analytical solution is considered to initiate the code. To confirm these findings, a linear stability analysis (see § 4.2.3) of the analytical solution is carried out for $Ra_T = -2 \times Ra^{sup}$, $Ra_S = -3 \times Ra^{sup}$, $Le = 10$ and $Pr = 7$ ($Ra^{sup} = 720$). For Neumann boundary conditions, it was found that, for the stable branch, all the eigenvalues have negative real parts for any wavelength. However, for the unstable branch, the solution was found to be unstable to perturbations having a wavelength greater than 1.94. For this situation, it was found that at least two eigenvalues have positive real parts (the imaginary parts are zero). The maximum eigenvalue real part, $p_r = 2.26$, is reached at $A = 2.72$. These results indicate clearly that the upper solution is stable and the lower one is unstable which is in agreement with the nonlinear numerical prediction. Similar results, not presented here, are obtained for other situations (i.e. Dirichlet boundary conditions). Obviously, as discussed in § 4.2.3, for high Rayleigh number, the upper steady-state solution becomes unstable and a transition to oscillatory flow is expected to occur.

The transition from oscillatory to steady flow will be now examined in a container having a finite aspect ratio with non-slip boundaries for large value of $|Ra_S|$. The results are analysed in the range ($Ra_{TC}^{over} < Ra_T < Ra_{TC}^{osc}$). A qualitative comparison of the flow behaviour is made with results obtained by Huppert & Moore (1976) and Moore *et al.* (1991) in an infinite horizontal layer with stress-free horizontal

	Ra^{sup}	Ra_{TC}^{over} (Approximate)	Ra_{TC}^{over} (Accurate)	Ra_{TC}^{osc} (Approximate)	Ra_{TC}^{osc} (Accurate)
One-cell mode (λ_1)	2323	29 247	32 102	52 478	···
Two-cell mode (λ_2)	2716	28 337	31 616	55 515	55 492

TABLE 9. Critical Rayleigh numbers for $Ra_S = -10^5$, $Pr = 1$, $Le = 10^{1/2}$, $A = 1.5$ and $a = 0$. The mesh size is 12×10.

boundaries. In their studies, the solution domain is restricted to a rectangular cavity with the half-wavelength as an aspect ratio, using stress-free and impermeable vertical walls. In the overstable regime, it was demonstrated that the oscillatory flow is characterized by a cyclically reversed flow circulation. Due to the impermeable lateral boundary conditions considered by these authors, the convective cells were found to be always constrained in the solution domain. However, using correct periodic boundary conditions, Deane *et al.* (1987) and Spina *et al.* (1998) have demonstrated that, in the oscillatory regime, the flow motion is characterized by standing, travelling, modulated and/or chaotic waves. To examine the influence of non-slip boundary conditions on the flow behaviour, some results have been obtained for $A = 1.5$, $Ra_S = -10^5$, $Pr = 1$, $Le = 10^{1/2}$ and $a = 0$. For this situation, the critical Rayleigh numbers according to the linear stability analysis, are given in Table 9. For the value $A = 1.5$ chosen here, the linear stability results reveal that at least two convective modes can coexist. Among these, there are one-cell and two-cell modes which correspond to the first two eigenvalues (λ_1 and λ_2, respectively; for similar results see figure 1*a*).

The numerical solutions of the full governing equations are obtained for a grid 24×20 and time step $\Delta t = 2 \times 10^{-4}$. The grid and the time step chosen here were found to be sufficient to capture the transient flow details. Obviously, this requires large computation times. In the absence of nonlinear effects, the linear stability analysis stipulates that the overstable regime lies between approximately $Ra_T = 29\,000$ and 55 000. However, the numerical solution shows that at $Ra_T = 40\,000$ the flow is steady and symmetric. As indicated in figure 14(*a*) and 14(*b*), at least two solutions are possible, namely the one-cell and two-cells modes.

The one-cell mode will be considered first. By decreasing Ra_T progressively to 35 500, the flow is observed to decrease in intensity and lose its spatial symmetry slightly. Depending on the flow circulation (clockwise here), the cell is shifted progressively to the right and almost a quiescent flow (very weak clockwise circulation) exists in the left part of the container. This behaviour is illustrated in figure 14(*c*). When Ra_T is decreased to 35 000, as shown in figure 15, the solution becomes unsteady and it is characterized by asymmetric multicellular flows in which the rolls are moving non-uniformly from left to right in an oscillatory manner. Similar results were obtained by Huppert & Moore (1976). For this situation, the time history of the heat and mass transfer rates (Nu_m and Sh_m) indicates clearly that the flow is periodically oscillating and exhibits six extremums per period.

Upon decreasing the value of Ra_T down to 32 000, the numerical solution indicates that the travelling cells observed for $Ra_T = 35\,000$ are transformed into oscillatory standing rolls for which the flow circulation is reversed cyclically. As depicted in figure 16, the cell number varies from one to three and the time history of Nu_m and Sh_m indicates that these parameters exhibit six and four extremums respectively within each period. Below $Ra_T = 30\,000$, a decaying flow is observed. For this case, the effect

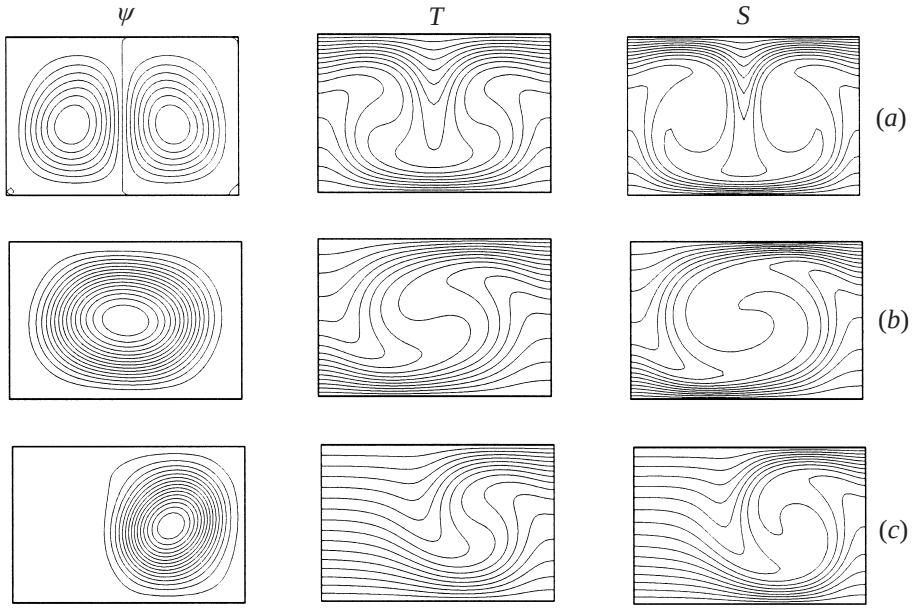

FIGURE 14. Steady flows for $Ra_S = -10^5$, $Pr = 1$, $Le = 10^{1/2}$ and $a = 0$. (*a*) Two-cell mode: $Ra_T = 40\,000$, $\psi_{max} = 10.126$, $\psi_{min} = -10.126$, $Nu_m = 2.546$ and $Sh_m = 3.741$. (*b*) One-cell mode: $Ra_T = 40\,000$, $\psi_{max} = 15.539$, $\psi_{min} = -0.022$, $Nu_m = 2.442$ and $Sh_m = 3.535$. (*c*) One-cell mode: $Ra_T = 35\,500$, $\psi_{max} = 8.863$, $\psi_{min} = -0.339$, $Nu_m = 1.697$ and $Sh_m = 2.316$.

of the enclosure aspect ratio, A, on the travelling waves has also been investigated numerically. As discussed above, for $Ra_T = 35\,000$ and $A = 1.5$, the oscillatory flow is characterized by asymmetric cells moving in the horizontal direction. By decreasing progressively the aspect ratio step by step ($\Delta A = 0.1$) it was found that the travelling cells can be sustained down to $A = 1.3$. However, for $A = 1.2$, the convective flows become steady, symmetric and unicellular (not presented here).

The two-cell mode is now considered. Upon decreasing the Rayleigh number progressively from 40 000, and using the previous solution as initial conditions, this type of flow pattern was found to hold approximately down to $Ra_T = 33\,000$. Below that value, the flow becomes oscillatory as illustrated in figure 16. However, upon using a two-cell steady mode (obtained for $Ra_T = 35\,000$) as initial conditions for $Ra_T = 30\,000$, the numerical solution indicates the occurrence of another kind of oscillatory flow that can be maintained down to $Ra_T = 29\,500$ (see figure 17). The flow structure now consists of two to six counter-rotating rolls and the flow circulation is reversing cyclically. For this situation, either Nu_m and Sh_m (figure 17*a*) exhibit four extrema. Using this solution as initial conditions for $Ra_T > 30\,000$, the numerical results indicate that this oscillatory behaviour is broken and leads to another unsteady periodic flow as shown in figure 18 for $Ra_T = 32\,000$ which is very different from that observed in figure 16. In this range, a small hysteresis loop between the two solutions was found to exist. Also, it is noticed that, according to the above results and the linear stability analysis, convective flows are possible below the threshold for oscillatory convection.

In all the above results, the oscillatory flows are periodic. In the past, Huppert & Moore (1976) and Moore *et al.* (1991) have observed that the transition from oscillatory to steady flow occurs through the appearance of asymmetric and aperiodic solutions. However, using periodic boundary conditions, Deane *et al.* (1987) have

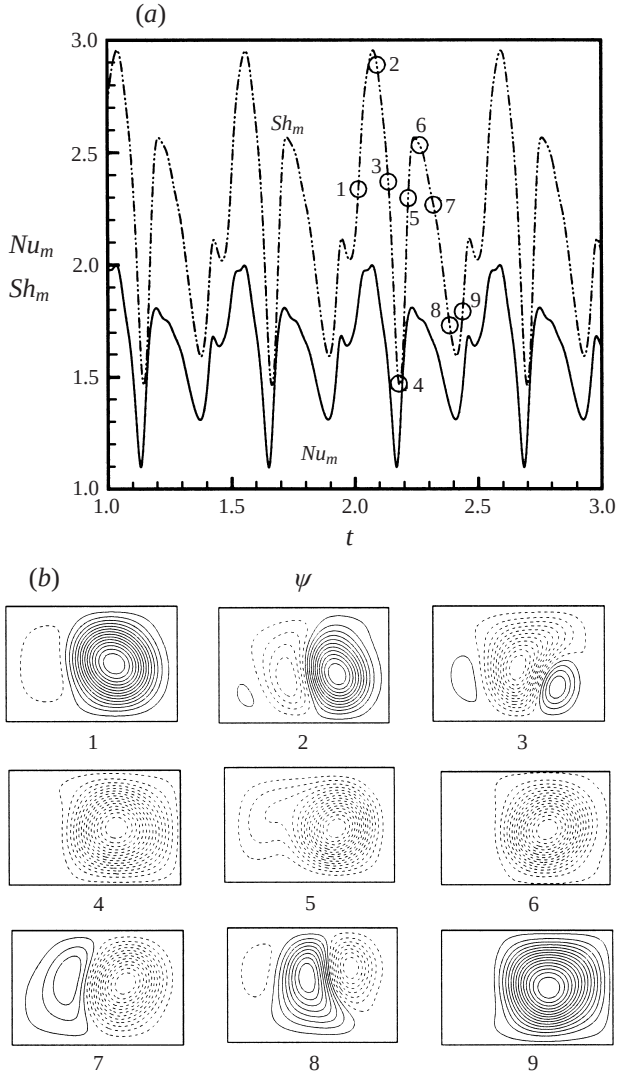

FIGURE 15. Oscillatory flows for $Ra_T = 35\,000$, $Ra_S = -10^5$, $Pr = 1$, $Le = 10^{1/2}$ and $a = 0$: (*a*) time history of the Nusselt number, Nu_m, and Sherwood number, Sh_m; (*b*) time evolution of the flow structure.

demonstrated that aperiodic (chaotic) convection occurs just near the threshold of the overstability. Far above this threshold, before achieving the steady-state solution, the flows are characterized by waves travelling at constant velocity which vanish linearly as Ra_T is increased. In the present study, using the oscillatory periodic solution obtained for $Ra_T = 35\,000$ and $A = 1.5$ (figure 16), it is found numerically that aperiodic flows exist within a narrow range of Ra_T (approximately for $35\,250 < Ra_T < 35\,750$, the results are not presented here).

In general, the present results obtained in rigid containers with an aspect ratio of $A = 1.5$ are qualitatively the same as those presented by Huppert & Moore (1976) in an infinite enclosure with stress-free boundaries. To simulate the periodicity of the flow structure in the horizontal direction, an aspect ratio equal to half of the critical wavelength at the onset of convection was chosen by these authors. Due to

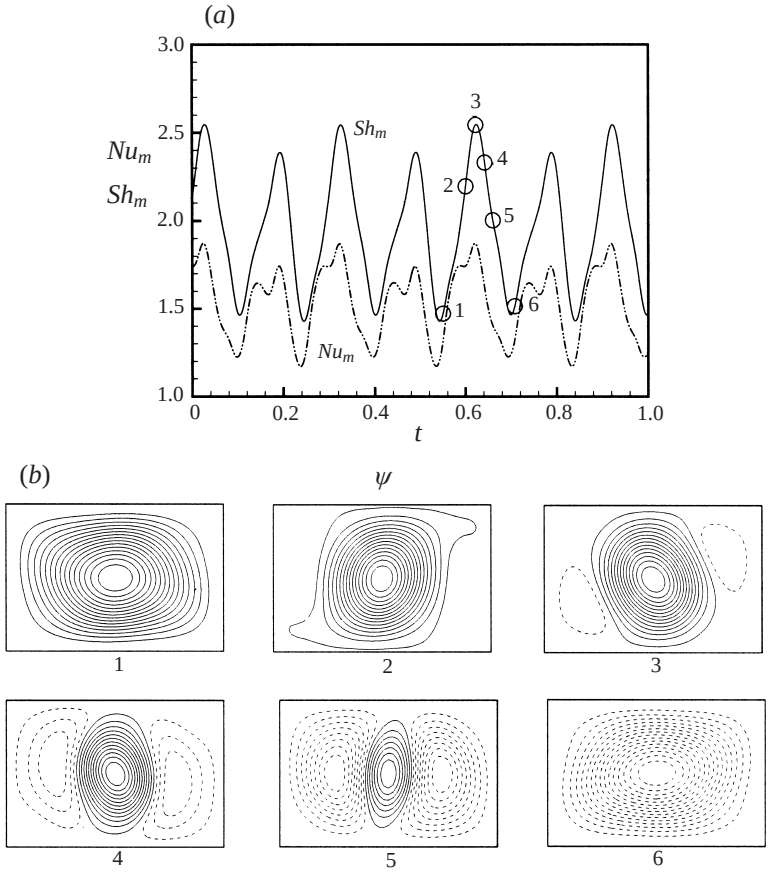

FIGURE 16. As figure 15 but $Ra_T = 32\,000$.

an inappropriate periodic boundary condition, i.e. impermeable stress-free vertical boundaries, the convective cells were not allowed to move in the horizontal direction. In fact, it was found in the present study and in those by Deane *et al.* (1987) and Spina *et al.* (1998) that when using a correct periodic boundary condition, the oscillatory flows could be characterized by travelling waves in the horizontal direction. Therefore, the boundary conditions considered by Huppert & Moore (1976) could be suitable for steady or oscillatory convective flows (standing waves) when the lateral roll boundaries are vertical. In general the results presented by Huppert & Moore (1976) describe very well convective flows in a finite aspect ratio container. Also, it was noted that in an infinite layer with stress-free boundaries, the critical wavelength at the onset of monotonic and oscillatory convection is the same. This is not the case in enclosures having rigid boundaries as discussed in the present paper.

The present study concerns double-diffusive convection in clear fluid media and it is similar to that conducted by Mamou & Vasseur (1999) in porous media. In general, the results of both studies are found to be qualitatively the same near the threshold of oscillatory convection and even far away from criticality. For large Prandtl numbers ($Pr \gg 1$) in fluid media (the inertial forces are negligible which is the case in Darcy porous media), the same expressions are obtained by Mamou & Vasseur (1999) for the thresholds of subcritical, oscillatory and monotonic convection (see (4.22)) when the normalized porosity of the porous media is equal to unity. For lower values of Pr

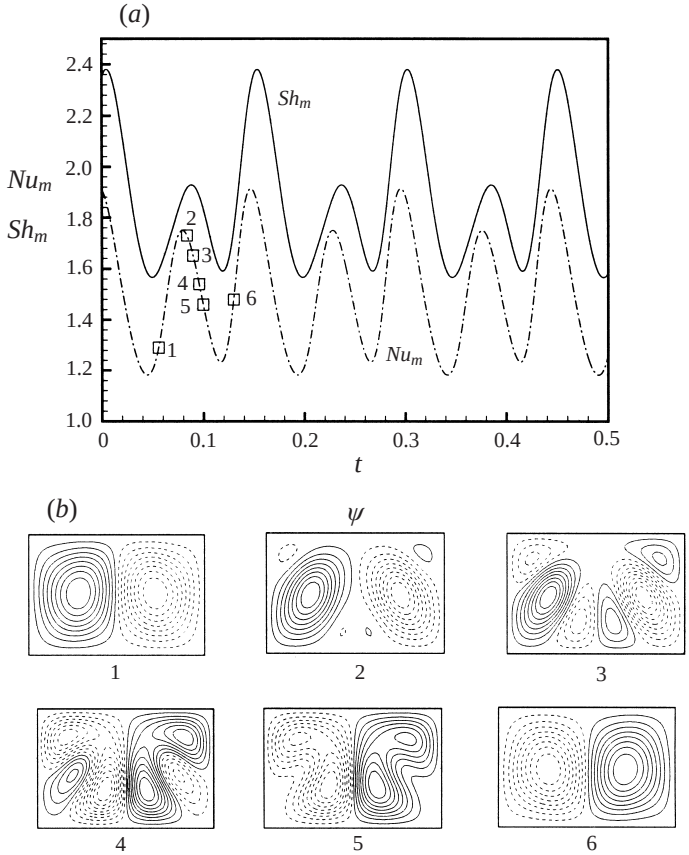

FIGURE 17. As figure 15 but $Ra_T = 30\,000$.

(inertial force are significant) it is expected that the convective flow behaviour in a fluid medium could be very different from that in the porous medium. In an infinite enclosure, with Dirichlet boundary conditions, the critical wavelength at the onset of overstabilities is different from that of the onset of monotonic convection and it was found to be a function of the governing parameters. However, in a porous medium, the critical wavelength is constant ($A_C = 2$). On the other hand, for Neumann boundary conditions, the critical wavelength is infinite for the porous medium while it could be finite for the fluid medium, depending on the governing parameter values.

6. Conclusion

The present paper is devoted to numerical and analytical experiments on double-diffusive convection in confined enclosures subject to vertical gradients of temperature and solute. Interest in this type of problem is motivated by its importance in many situations such as in chemical engineering and metallurgy where convection in multi-component fluids is involved. The vertical walls of the cavity are assumed rigid, insulated and impermeable, while rigid and stress-free horizontal boundaries are considered. The vertical gradients of temperature and solute are established by maintaining the horizontal boundaries at fixed temperatures and solute concentrations (Dirichlet type) or by imposing constant fluxes of heat and solute on these boundaries (Neumann type).

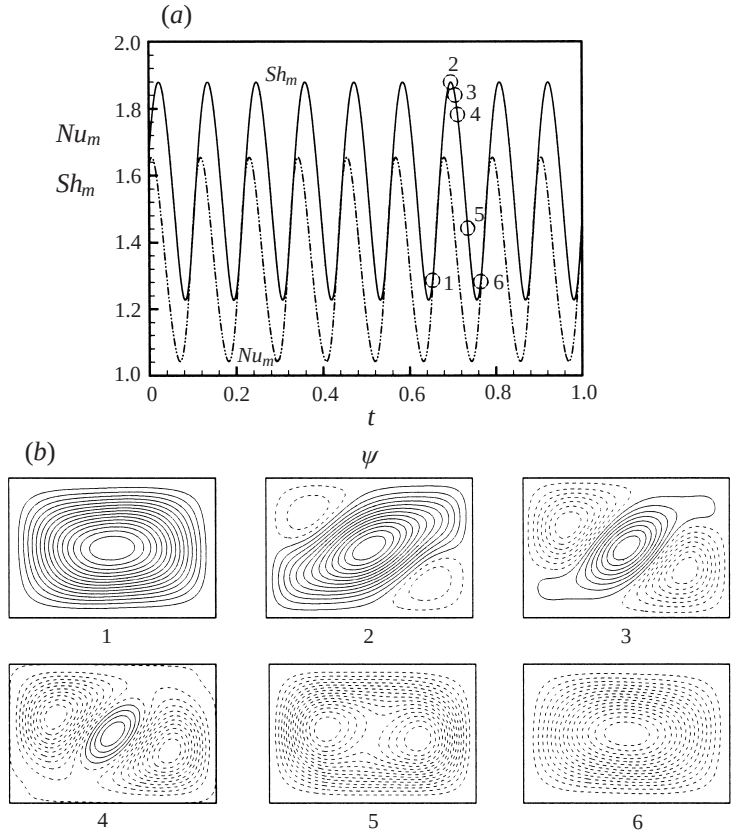

FIGURE 18. As figure 15 but $Ra_T = 32\,000$.

The partial differential governing equations are integrated numerically using a finite element method. Reliable numerical techniques are developed, on the basis of Galerkin and finite element methods, to study the linear stability of the system by considering various boundary conditions. Using the Galerkin method, a weak nonlinear stability analysis is also carried out to investigate the possible existence of convective flows below the threshold of monotonic instabilities. The main conclusions of the present investigation are summarized here below.

When the solute is stabilizing, the linear stability analysis indicates that subcritical flows are possible and the thresholds for stationary, oscillatory and subcritical convection are determined in terms of the governing parameter. For an infinite layer with non-slip boundaries, it was found that the critical wavelength is a function of the governing parameters for both Dirichlet and Neumann boundary conditions and travelling waves were found to occur near the threshold of oscillatory convection.

On the other hand, as predicted by the nonlinear solution, various phenomena have been observed, especially below the threshold of monotonic instability, such as oscillatory periodic or aperiodic flows with complex flow structures. In a square enclosure, the flow was found to evolve cyclically from clockwise to counterclockwise circulation and vice versa. For a shallow confined enclosure (relatively large aspect ratio), the oscillatory flow patterns are non-symmetric and they are characterized by horizontal travelling waves. In an infinite horizontal layer, using periodic boundary conditions, standing and travelling waves have been observed.

Far from criticality, a stability analysis of the parallel flow solution is carried out and the threshold for Hopf bifurcation (transition from steady to unsteady states) is obtained. Within the range of the governing parameters considered in the present study, good agreement is obtained between the analytical and the nonlinear numerical results.

The authors are grateful to the reviewers of the manuscript for their constructive criticisms and useful comments which have improved significantly the general quality of the present study. We also would like to thank Dr Ali Benmeddour for his helpful comments and suggestions on this work.

Appendix A. Numerical solution

The weak Galerkin formulation of the governing equations (2.1) is obtained as follows:

$$\frac{\partial}{\partial t}\left(\int_\Omega \nabla\psi\cdot\nabla w\,\mathrm{d}\Omega-\int_\Gamma \frac{\partial\psi}{\partial \boldsymbol{n}}w\,\mathrm{d}\Gamma\right)+\int_\Omega J(\psi,\nabla^2\psi)w\,\mathrm{d}\Omega+Pr\left(\int_\Omega \nabla^2\psi\cdot\nabla^2 w\,\mathrm{d}\Omega\right.$$
$$\left.-\int_\Gamma \nabla^2\left(\frac{\partial\psi}{\partial\boldsymbol{n}}\right)w\,\mathrm{d}\Gamma+\int_\Gamma \nabla^2\psi\frac{\partial w}{\partial\boldsymbol{n}}\,\mathrm{d}\Gamma\right)=Pr\int_\Omega\left(Ra_T\frac{\partial\theta}{\partial x}+\frac{Ra_S}{Le}\frac{\partial\phi}{\partial x}\right)w\,\mathrm{d}\Omega, \quad (A\,1)$$

$$\frac{\partial}{\partial t}\int_\Omega \theta\vartheta\,\mathrm{d}\Omega+\int_\Omega\frac{\partial\psi}{\partial x}\vartheta\,\mathrm{d}\Omega-\int_\Omega J(\psi,\theta)\vartheta\,\mathrm{d}\Omega=-\int_\Omega\nabla\theta\cdot\nabla\vartheta\,\mathrm{d}\Omega+\int_\Gamma\frac{\partial\theta}{\partial\boldsymbol{n}}\vartheta\,\mathrm{d}\Gamma, \quad (A\,2)$$

$$\frac{\partial}{\partial t}\int_\Omega \phi\vartheta\,\mathrm{d}\Omega+\int_\Omega\frac{\partial\psi}{\partial x}\vartheta\,\mathrm{d}\Omega-\int_\Omega J(\psi,\phi)\vartheta\,\mathrm{d}\Omega=\frac{1}{Le}\left(-\int_\Omega\nabla\phi\cdot\nabla\vartheta\,\mathrm{d}\Omega+\int_\Gamma\frac{\partial\phi}{\partial\boldsymbol{n}}\vartheta\,\mathrm{d}\Gamma\right), \quad (A\,3)$$

respectively, where w and ϑ are the weighted admissible functions, $\boldsymbol{n}$ is the outward boundary normal vector, Ω is the flow field domain and Γ its boundary.

The elementary matrices for the linear system of (3.1)–(3.3) are

$$\left.\begin{aligned}
[\boldsymbol{B}]^e &= \int_{\Omega^e}\frac{\partial\mathscr{H}_j}{\partial x}\mathscr{H}_i\,\mathrm{d}\Omega^e,\\
[\boldsymbol{C}_\theta]^e=[\boldsymbol{C}_\phi]^e=[\boldsymbol{C}]^e &= \int_{\Omega^e}J(\psi^n_{k-1},\mathscr{H}_j)\mathscr{H}_i\,\mathrm{d}\Omega^e,\\
[\boldsymbol{K}_\theta]^e=[\boldsymbol{K}_\phi]^e=[\boldsymbol{K}]^e &= \int_{\Omega^e}\nabla\mathscr{H}_j\cdot\nabla\mathscr{H}_i\,\mathrm{d}\Omega^e,\\
[\boldsymbol{M}_\psi]^e &= \int_{\Omega^e}\nabla\mathscr{H}_j\cdot\nabla\mathscr{H}_i\,\mathrm{d}\Omega^e,\\
[\boldsymbol{C}_\psi]^e &= \int_{\Omega^e}J(\psi^n_{k-1},\nabla^2\mathscr{H}_j)\mathscr{H}_i\,\mathrm{d}\Omega^e,\\
[\boldsymbol{K}_\psi]^e &= \int_{\Omega^e}\nabla^2\mathscr{H}_j\cdot\nabla^2\mathscr{H}_i\,\mathrm{d}\Omega^e,\\
[\boldsymbol{L}_\theta]^e=[\boldsymbol{L}_\phi]^e=[\boldsymbol{L}]^e &= -\int_{\Omega^e}\frac{\partial\mathscr{H}_j}{\partial x}\mathscr{H}_i\,\mathrm{d}\Omega^e,\\
[\boldsymbol{M}_\theta]^e=[\boldsymbol{M}_\phi]^e=[\boldsymbol{M}]^e &= \int_{\Omega^e}\mathscr{H}_j\mathscr{H}_i\,\mathrm{d}\Omega^e,
\end{aligned}\right\} \quad (A\,4)$$

where Ω^e is the integration domain of a given element and $\mathscr{H}_i$ are the Hermite interpolation functions. The above integrals are computed accurately by using the Gauss formulae.

Appendix B. Stability analysis

For an infinite layer the elementary matrices are obtained as follows:

$$[\boldsymbol{B}]^e = \mathrm{i}\omega \int_{\Delta z_e} \mathscr{H}_j \mathscr{H}_i \, \mathrm{d}z,$$

$$[\boldsymbol{L}]^e = -\mathrm{i}\omega \int_{\Delta z_e} \mathscr{H}_j \mathscr{H}_i \, \mathrm{d}z,$$

$$[\boldsymbol{M}_\psi]^e = \int_{\Delta z_e} \left(\frac{\mathrm{d}\mathscr{H}_j}{\mathrm{d}z} \frac{\mathrm{d}\mathscr{H}_i}{\mathrm{d}z} + \omega^2 \mathscr{H}_j \mathscr{H}_i \right) \mathrm{d}z,$$

$$[\boldsymbol{K}]^e = \int_{\Delta z_e} \left(\frac{\mathrm{d}\mathscr{H}_j}{\mathrm{d}z} \frac{\mathrm{d}\mathscr{H}_i}{\mathrm{d}z} + \omega^2 \mathscr{H}_j \mathscr{H}_i \right) \mathrm{d}z,$$

$$[\boldsymbol{K}_\psi]^e = \int_{\Delta z_e} \left(\frac{\mathrm{d}^2\mathscr{H}_j}{\mathrm{d}z^2} \frac{\mathrm{d}^2\mathscr{H}_i}{\mathrm{d}z^2} + 2\omega^2 \frac{\mathrm{d}\mathscr{H}_j}{\mathrm{d}z} \frac{\mathrm{d}\mathscr{H}_i}{\mathrm{d}z} + \omega^4 \mathscr{H}_j \mathscr{H}_i \right) \mathrm{d}z,$$

$$[\boldsymbol{M}_\theta]^e = [\boldsymbol{M}_\phi]^e = [\boldsymbol{M}]^e = \int_{\Delta z_e} \mathscr{H}_j \mathscr{H}_i \, \mathrm{d}z,$$

where $\mathscr{H}_i(z)$ are the one-dimensional Hermite cubic interpolation functions. The dimension of the global matrices is reduced to $m_z \times m_z$ with $m_z = 2(N_{ez} + 1)$.

Appendix C. Weak nonlinear theory

The constants in (4.11)–(4.13) and (4.26)–(4.28) are given by the following integrals:

$$\mathscr{B} = \int_\Omega \frac{\partial G}{\partial x} F \, \mathrm{d}\Omega, \qquad \mathscr{K} = \int_\Omega (\nabla G)^2 \, \mathrm{d}\Omega, \qquad \mathscr{K}_\psi = \int_\Omega (\nabla^2 F)^2 \, \mathrm{d}\Omega,$$

$$\mathscr{L} = -\int_\Omega \frac{\partial F}{\partial x} G \, \mathrm{d}\Omega, \quad \mathscr{M} = \int_\Omega G^2 \, \mathrm{d}\Omega, \qquad \mathscr{M}_\psi = \int_\Omega (\nabla F)^2 \, \mathrm{d}\Omega,$$

$$\mathscr{K}_1 = \int_\Omega (\nabla h)^2 \, \mathrm{d}\Omega, \qquad \mathscr{L}_1 = -\int_\Omega \frac{\partial F}{\partial x} \frac{\mathrm{d}h}{\mathrm{d}z} G \, \mathrm{d}\Omega, \quad \mathscr{L}_2 = \int_\Omega J(F, G) h \, \mathrm{d}\Omega,$$

$$\mathscr{M}_1 = \int_\Omega h^2 \, \mathrm{d}\Omega.$$

These integrals were performed with a finite element method using the cubic Hermite element.

Appendix D. Stability analysis of the asymptotic solution

The elementary matrices of the linear system resulting from the numerical discretization of (4.38), are given by

$$[\mathbb{B}_\theta]^e = \left([\boldsymbol{B}]^e - \mathrm{i}\omega \int_{\Delta z_e} \frac{\mathrm{d}\theta_b}{\mathrm{d}z} \mathscr{H}_j \mathscr{H}_i \,\mathrm{d}z\right) + C_T \int_{\Delta z_e} \frac{\mathrm{d}\mathscr{H}_j}{\mathrm{d}z} \mathscr{H}_i \,\mathrm{d}z, \qquad [\mathbb{B}_{\psi\theta}]^e = -\mathrm{i}\omega Pr Ra_T [\boldsymbol{B}]^e,$$

$$[\mathbb{B}_\phi]^e = \left([\boldsymbol{B}]^e - \mathrm{i}\omega \int_{\Delta z_e} \frac{\mathrm{d}\phi_b}{\mathrm{d}z} \mathscr{H}_j \mathscr{H}_i \,\mathrm{d}z\right) + C_S \int_{\Delta z_e} \frac{\mathrm{d}\mathscr{H}_j}{\mathrm{d}z} \mathscr{H}_i \mathrm{d}z, \qquad [\mathbb{B}_{\psi\phi}]^e = -\mathrm{i}\omega Pr \frac{Ra_S}{Le} [\boldsymbol{B}]^e,$$

$$[\mathbb{K}_\theta]^e = [\boldsymbol{K}]^e + \mathrm{i}\omega \int_{\Delta z_e} \frac{\mathrm{d}\psi_b}{\mathrm{d}z} \mathscr{H}_j \mathscr{H}_i \,\mathrm{d}z,$$

$$[\mathbb{K}_\psi]^e = Pr[\boldsymbol{K}_\psi]^e + \mathrm{i}\omega \int_{\Delta z_e} \left[\left(\frac{\mathrm{d}^3\psi_b}{\mathrm{d}z^3} + \omega^2 \frac{\mathrm{d}\psi_b}{\mathrm{d}z}\right) \mathscr{H}_j - \frac{\mathrm{d}\psi_b}{\mathrm{d}z} \frac{\mathrm{d}^2\mathscr{H}_j}{\mathrm{d}z^2}\right] \mathscr{H}_i \,\mathrm{d}z,$$

$$[\mathbb{K}_\phi]^e = \frac{1}{Le}[\boldsymbol{K}]^e + \mathrm{i}\omega \int_{\Delta z_e} \frac{\mathrm{d}\psi_b}{\mathrm{d}z} \mathscr{H}_j \mathscr{H}_i \,\mathrm{d}z, \qquad [\mathbb{M}_\psi]^e = -[\boldsymbol{M}_\psi]^e,$$

$$[\mathbb{M}_\theta]^e = -[\boldsymbol{M}_\theta]^e, \qquad [\mathbb{M}_\phi]^e = -[\boldsymbol{M}_\phi]^e,$$

where $[\boldsymbol{B}]^e$, $[\boldsymbol{M}_\psi]^e$, $[\boldsymbol{M}_\theta]^e$, $[\boldsymbol{M}_\phi]^e$, $[\boldsymbol{K}_\psi]^e$, $[\boldsymbol{K}_\theta]^e$ and $[\boldsymbol{K}_\phi]^e$ are defined in Appendix B.

REFERENCES

Ahlers, G. & Lücke, M. 1987 Some properties of an eight-mode Lorentz model for convection in binary fluids. *Phys. Rev.* A **35**, 470–473.

Baines, P. G. & Gill, A. E. 1969 On the thermohaline convection with linear gradients. *J. Fluid Mech.* **37**, 289–306.

Cormack, D. E., Leal, L. G. & Imberger, J. 1974 Natural convection in a shallow cavity with differentially heated end walls. Part 1. Asymptotic theory. *J. Fluid Mech.* **65**, 209–230.

Da Costa, L. N., Knobloch, E. & Weiss, N. O. 1981 Oscillations in double-diffusive convection. *J. Fluid Mech.* **109**, 25–43.

Deane, A. E., Knobloch, E. & Toomre, J. 1987 Traveling waves and chaos in thermosolutal convection. *Phys. Rev.* A **36**, 2862–2869.

Howard, L. N. & Veronis, G. 1992 Stability of salt fingers with negligible diffusivity. *J. Fluid Mech.* **239**, 511–522.

Huppert, H. E. & Moore, D. R. 1976 Nonlinear double-diffusive convection. *J. Fluid Mech.* **78**, 821–854.

Huppert, H. E. & Turner, J. S. 1981 Double-diffusive convection. *J. Fluid Mech.* **106**, 299–329.

Kimura, S., Vynnycky, M. & Alavyoon, F. 1995 Unicellular natural circulation in a shallow horizontal porous layer heated from below by a constant flux. *J. Fluid Mech.* **294**, 231–257.

Knobloch, E. & Moore, D. R. E. 1988 Linear stability of experimental Soret convection. *Phys. Rev.* A **37**, 860–867.

Knobloch, E. & Proctor, M. R. E. 1981 Nonlinear periodic convection in double-diffusive systems. *J. Fluid Mech.* **108**, 291–316.

Lieber, P. & Rintel, L. 1963 Convective instability of a horizontal layer of fluid with maintained concentration of diffusive substance and temperature on the boundaries. *Rep.* MD-6, Inst. Engng Res., Univ. of Calif., Berkeley.

Mamou, M. & Vasseur, P. 1999 Thermosolutal bifurcation phenomena in porous enclosures subject to vertical temperature and concentration gradients. *J. Fluid Mech.* **395**, 61–87.

Mamou, M., Vasseur, P. & Bilgen, E. 1996 Analytical and numerical study of double diffusive convection in a vertical enclosure. *Heat Mass Transfer* **32**, 115–125.

Mamou, M., Vasseur, P. & Bilgen, E. 1998 Double diffusive instability problem in a vertical porous enclosure. *J. Fluid Mech.* **368**, 263–289.

Moore, D. R., Weiss, N. O. & Wilkins, J. M. 1991 Asymmetric oscillations in thermosolutal convection. *J. Fluid Mech.* **233**, 561–585.

Nield, D. A. 1967 The thermohaline Rayleigh–Jeffreys problem. *J. Fluid Mech.* **29**, 545–558.

Platten, J. K. & Legros, J. C. 1984 *Convection in Liquids*. Springer.

Predtechensky, A. A., McCormick, W. D., Swiff, J. B., Rossberg A. G. & Swinney, H. L. 1994 Traveling wave instability in sustained double-diffusive convection. *Phys. Fluids* **6**, 3923–3935.

Proctor, M. R. E. 1981 Steady subcritical thermohaline convection. *J. Fluid Mech.* **105**, 507–521.

Rayleigh, L. 1916 On convection currents in a horizontal layer of fluid when the higher temperature is on the under side. *Phil. Mag.* **32**, 529–546.

Reddy, J. N. 1993 *An Introduction to the Finite Element Method*. McGraw-Hill.

Reid, W. H. & Harris, D. L. 1958 Some further results on the Bénard problem. *Phys. Fluids* **1**, 102–110.

Sparrow, E. M., Goldstein, R. J. & Jonsson, V. K. 1964 Thermal instability in a horizontal fluid layer: effect of boundary conditions and nonlinear temperature profile. *J. Fluid Mech.* **18**, 513–528.

Spina, A., Toomre, J. & Knobloch, E. 1998 Confined states in large-aspect-ratio thermosolutal convection. *Phys. Rev.* E **57**, 524–545.

Stern, M. E. 1960 The 'salt fountain' and thermohaline convection. *Tellus* **12**, 172–175.

Turner, J. S. 1985 Multicomponent convection. *Ann. Rev. Fluid Mech.* **17**, 11–44.

Veronis, G. 1965 On finite amplitude instability in thermohaline convection. *J. Mar. Res.* **23**, 1–17.

Veronis, G. 1968 Effect of a stabilizing in thermohaline convection. *J. Fluid Mech.* **34**, 315–368.